Systems-level analysis predicts no autotrophy-linked protein-RNA interactions in Clostridium autoethanogenum

nature communications

Article

https://doi.org/10.1038/s41467-026-75309-w

Systems-level analysis predicts no autotrophy-linked protein-RNA interactions in *Clostridium autoethanogenum*

Received: 23 December 2025

Accepted: 22 June 2026

Published online: 08 July 2026

Check for updates

Angela Re[1] ✉, Gianfranco Michele Maria Politano[2], Kristina Reinmets[3], Alfredo Benso[2], Laurence Girbal[4], Muriel Cocaign-Bousquet[4] & Kaspar Valgepea[3] ✉

Burning fossil fuels drives climate change with detrimental consequences on humankind while waste accumulation from increasing consumption threatens biosustainability globally. Gas fermentation enables to recycle carbon oxides (CO and CO_2) from industrial waste gases and gasified waste into value-added products using gas-fermenting microbes, namely acetogens. However, our limited understanding of gene function and metabolic regulation is hindering rational engineering of acetogen cell factories. In this work, we aimed to identify genome-wide protein-RNA interactions contributing to autotrophy in the model-acetogen *Clostridium autoethanogenum* by combining steady-state chemostat cultivation, functional genomics, and computational methods. We first detected limited and uncoupled transcriptional and translational regulation between autotrophy and heterotrophy. Rigorous mapping of genome-wide transcriptional architecture revealed both differential usage and signal strength of transcriptional start and termination sites between genes and growth substrates. We then used computational tools to reconstruct protein-RNA interactions for differentially regulated genes, predicting 14 trans-acting regulatory RNA-binding proteins (RBPs) involved in post-transcriptional regulation but not linked to genes key for autotrophy. Most RBPs, one of which is translationally regulated, perform RNA modifications and regulate mRNA stability while others target translation-related genes. Our work provides valuable knowledge for metabolic engineering of acetogens and potentially contributes towards understanding primordial life on Earth.

Our continued reliance on fossil fuels drives greenhouse gas emissions that are accelerating climate change with detrimental consequences on the environment and humankind. In addition, increasing accumulation of waste from increasing global population and prosperity is threatening biosustainability through degradation of ecosystems. Gas fermentation has emerged as an attractive technology to tackle these challenges by recycling waste carbon from industrial off-gases and gasified waste into value-added products using gas-fermenting microbes[1,2]. Acetogens are the preferred biocatalysts for capture and conversion of carbon oxides (CO and CO_2) into fuels and chemicals[3,4] as they can use gas as their sole carbon and energy source[5] by employing the most-efficient CO_2-fixation pathway known to date[6,7],

[1]Department of Applied Science and Technology, Politecnico di Torino, Torino, Italy. [2]Department of Control and Computer Engineering, Politecnico di Torino, Torino, Italy. [3]Institute of Bioengineering, University of Tartu, Tartu, Estonia. [4]TBI, CNRS, INRAE, INSA, Université de Toulouse, Toulouse, France.
✉e-mail: angela.re@polito.it; kaspar.valgepea@ut.ee

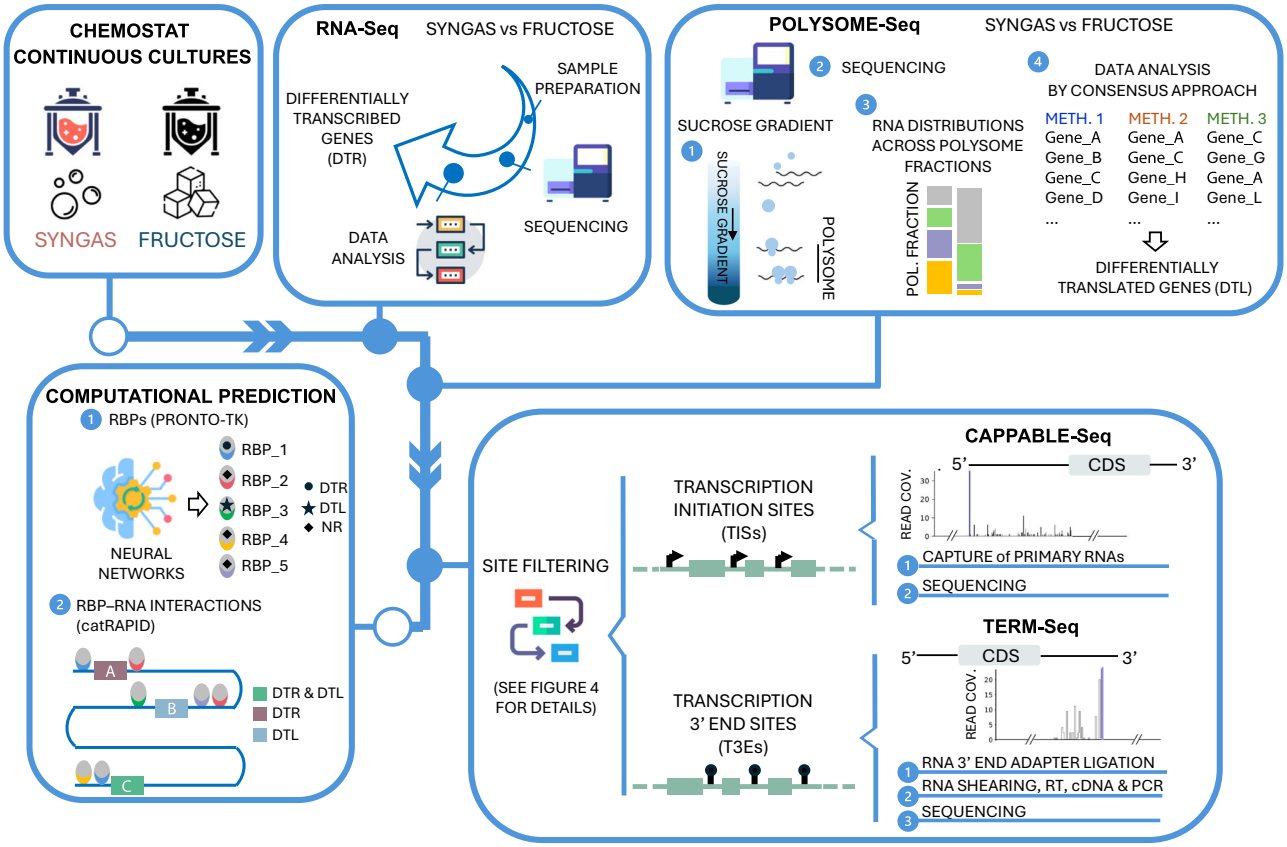

Fig. 1 | Integrative functional genomics and computational approach used in this work to predict RNA-binding proteins (RBPs) and protein-RNA interactions in *C. autoethanogenum*. CDS coding DNA sequence, DTR differentially transcribed, DTL differentially translated, NR not differentially regulated. This figure has been designed using resources from Flaticon.com (see Acknowledgements for complete source attribution).

the Wood-Ljungdahl pathway (WLP)[5,8]. However, our limited understanding of gene function and metabolic regulation in acetogens is hindering rational engineering of acetogen cell factories[3,4,9–11].

Most studies aimed at elucidating the relationship between genotypes and phenotypes in acetogens have focused on transcription[3]. Results from a limited set of experimental conditions suggest that metabolic fluxes in acetogens are primarily regulated post-translationally[12–14]. However, comprehensive analysis of acetogen multi-omics datasets[15–18] highlights that post-transcriptional regulation of gene expression has a significant effect on the flow of genetic information from DNA to protein[19], in a similar way to other microbes[20]. Key players in post-transcriptional regulation in microbes are RNA-binding proteins (RBPs)[20], encompassing direct[21] or indirect[22] regulation of transcription[23–25], RNA turnover[26], and translation[23,27–29]. Additionally, RBPs can play key roles in regulating microbial metabolism through distinct RBP-RNA interactions[30,31]. While some RBPs have been characterized in Clostridia[32], no RBPs have been described in acetogens so far, and thus we also lack knowledge about RBP-RNA interactions. Hence, fundamental understanding of acetogen metabolism and potentially also engineering of cell factories could be advanced through uncovering the unexplored space of RBPs.

The aim of our work was to identify genome-wide RBP-RNA interactions that contribute to autotrophy in acetogens. We used the model-acetogen *Clostridium autoethanogenum* as its metabolism has been explored through numerous omics datasets[3,33–38]. In addition, it has been engineered to produce various non-native chemicals[3,39,40] and it is used in commercial-scale gas fermentation for ethanol production[2]. We first aimed to experimentally directly identify RBPs using the RNA interactome capture (RIC) technique[41] as it had been recently adapted for the microbe *Escherichia coli*[42], but after numerous attempts failed to engineer a *C. autoethanogenum* strain expressing a heterologous poly(A) polymerase that is needed for genome-wide RNA polyadenylation and pull-down in RIC. We thus employed an alternative comprehensive approach to predict RBPs and RBP-RNA interactions by combining functional genomics and computational methods (Fig. 1).

Our approach first quantified both genome-wide transcriptional and translational regulation to identify transcripts differentially transcribed and/or translated during autotrophy vs heterotrophy. Second, we quantified genome-wide transcriptional architecture by accurate mapping of 5′-untranslated regions (UTR) and 3′UTRs at single-nucleotide resolution to determine the RNA sequences where RBPs most likely bind[43,44]. Last, we used the neural network-based toolkit PRONTO-TK[45] to predict potential RBPs and the inferential tool *cat*RAPID[46] to computationally reconstruct RBP-RNA interactions in *C. autoethanogenum*. Importantly, all these analyses were performed from the same autotrophic and heterotrophic cultures that were grown in bioreactor chemostat cultures, thus yielding steady-state data that enable quantification of strictly defined and condition-dependent phenotypes[47,48].

In this work, while we detect limited and uncoupled transcriptional and translational regulation between autotrophy and heterotrophy, *C. autoethanogenum* shows both differential usage and signal strength of transcriptional start and termination sites between genes and growth substrates. Reconstruction of protein-RNA interactions predicts 14 trans-acting regulatory RBPs involved in post-transcriptional regulation of differentially regulated genes for autotrophy. Our work provides valuable knowledge and potential targets for metabolic engineering of acetogens and potentially contributes

towards understanding primordial life as the WLP could be the first biochemical pathway on Earth[49].

Results

Autotrophic and heterotrophic chemostat cultures of *C. autoethanogenum*

To map genome-wide RBP-RNA interactions that could contribute to autotrophy in acetogens, we grew the *C. autoethanogenum* strain LAbrini[36] on syngas (CO, H_2, CO_2; i.e., autotrophically) and fructose (i.e., heterotrophically) in chemostat continuous cultures (Fig. 1). Importantly, this allowed us to grow cells at the same specific growth rate (μ; ~0.04 h^{-1} or ~1 day^{-1}), as μ equals dilution rate at steady-state, and thus facilitated unequivocal quantification of transcriptional and translational patterns of autotrophy and heterotrophy without the confounding effects from different μ during exponential autotrophic and heterotrophic batch growth. For instance, from the 2,030 differentially expressed transcripts between *C. autoethanogenum* syngas and fructose batch cultures[50], ~24% were also differentially expressed with faster growth in autotrophic chemostat cultures[34].

Notably, we found that both specific acetate and ethanol production rates (mmol per gram of cell dry weight per day) were ~2.3-fold higher and the specific 2,3-butanediol production rate was 9-fold higher for syngas vs fructose steady-state cultures (Supplementary Fig. 1a). The former can be explained by a doubled allocation of carbon into biomass (Supplementary Fig. 1b) that is favored by the more energy-rich nutrient fructose while the latter shows the higher need to regenerate reducing equivalents with by-products during autotrophy when less biomass can be produced. Interestingly, both syngas and fructose chemostat cultures with the LAbrini strain showed only ~1.5-fold higher acetate production than ethanol (Supplementary Fig. 1a) while nearly no ethanol production was detected in fructose-grown batch cultures of *C. autoethanogenum* strain JA1-1[50].

Limited transcriptional and translational control involved in realizing autotrophy

We first quantified transcriptional regulation involved in autotrophy (Fig. 1) using RNA-seq (Supplementary Data 1) and translational regulation using polysome-seq (Supplementary Data 2) instead of Ribo-seq since only polysome-seq offers resolution at the level of each mRNA copy[51]. While our RNA-seq analysis quantified transcript levels for 3557 genes, polysome-seq analysis determined the translation status for 3875 genes on average across bio-replicates of syngas and fructose cultures. The reproducibility of bio-replicates across syngas and fructose cultures was estimated with Spearman's correlation coefficients of 0.99 and 0.71 for RNA-seq and polysome-seq data (Supplementary Figs. 2a and 3), respectively. Bio-replicates for RNA-seq data also clustered well showing clearly distinguished transcriptome profiles between syngas and fructose cultures (Supplementary Fig. 2b, c). Combined correlation analysis, compositional distance analysis, and principal component analysis of polysome-seq data (see Methods for details) led to the removal of an outlier bio-replicate culture for both syngas and fructose (Supplementary Fig. 4). Analysis of RNA-seq data yielded 1784 genes with statistically differential expression (q-value < 0.05) between syngas and fructose growth (Fig. 2a and Supplementary Data 3). We determined the top 5% ranking ones according to q-value (lower value ranks higher) as differentially transcribed genes (DTRs) to ensure consistency with determination of differentially translated genes (DTLs) from polysome-seq data (see next paragraph). Thus, 176 genes were considered as DTR with 109 and 67 being down- or up-regulated, respectively, on syngas vs fructose (Fig. 2a and Supplementary Data 3).

Since polysome-seq quantifies transcripts bound to different numbers of ribosomes at single mRNA copy level, it allows to capture distinct traits compared to Ribo-seq that are indicative of translational control. To take advantage of this for determining DTLs, we established three complementary metrics for translational regulation (Fig. 2b; see Methods for details). First, we calculated the ratio between the sum of the mRNA proportions quantified in the ribosome-bound and ribosome-free fractions per gene for both substrates. This is equivalent to the term ribosome occupancy traditionally used for polysome-seq data[51]. We then quantified the difference in this translation status metric between syngas and fructose (TL-STATUS) by subtracting the fructose ratio from the syngas one. Positive value for TL-STATUS thus indicates up-regulation and negative down-regulation on syngas vs fructose (Supplementary Data 4). Our data show that >90% of mRNA copies for each gene are ribosome-bound (Supplementary Data 2), similar to *E. coli*[52] but higher than in *Lactococcus lactis*[53] and *Saccharomyces cerevisiae*[51,54]. Second, we quantified the difference between the polysome profiles in the two growth conditions for each gene using the variance-weighted Aitchison's distance (TL-PROFILE) (Supplementary Data 4). Third, we quantified for each gene the number of polysome fractions for which the difference in mRNA proportions between syngas and fructose was statistically significant by bootstrapping (POLY-FRACTIONS) (Supplementary Data 4). While TL-STATUS captures the overall translation status of mRNAs for any gene, POLY-FRACTIONS and TL-PROFILE provide additional information on translational regulation by capturing differences between individual polysome fractions and their profiles, respectively.

To evaluate these three metrics as indicators of gene-level translational regulation involved in realizing autotrophy, we compared the genes within the top 5% ranks of each metric. From the total of 441 genes among the top 5% ranks, ~2% (8) and ~14% (61) were shared between three or two metrics, respectively (Fig. 2c). Interestingly, each metric identified ~29% (21.3, 32.2, 32.7%) unique genes and also unique KEGG Orthology (KO) functional categories[55] or Pfam entries[56] were enriched within the top 5% gene sets of each metric (Fig. 2d). Despite these limited overlaps at gene and functional class levels, cross-comparison of the top 5% gene sets across the three metrics showed that all three capture similar trends in translational regulation (Supplementary Methods; Supplementary Fig. 5). Therefore, we decided to determine DTLs using a CONSENSUS approach: firstly, we calculated for each gene its average rank across the three metrics; and secondly, we ranked these average ranks and defined DTLs as the genes in the top 5%. Accordingly, 186 genes were considered as DTLs, all of which were up-regulated on syngas vs fructose (Supplementary Data 4). We surmise that the latter result is a biological response as we used external RNA spike-ins in our polysome-seq approach to correct for technical variability in sample preparation (see Methods). Overall, DTLs covered 42% of all the genes among the top 5% ranks of the three metrics (Fig. 2c). Strong enrichment of translation-related genes in DTLs (Fig. 2e) is consistent with ribosomal proteins exerting self-regulation by autogenous repression[57].

Transcriptional and translational control for autotrophy are uncoupled

Comparing DTRs with DTLs revealed that ~47% of genes (166) were differentially regulated exclusively at transcript levels and ~50% (176) exclusively at the level of translation (Fig. 3a). While no DTLs were down-regulated on syngas vs fructose, the concordantly up-regulated six genes included the Fd-NAD^+ oxidoreductase Rnf complex subunit RsxC (LABRINI_16130; following gene IDs stated without "LABRINI_") and the NADH-quinone oxidoreductase complex subunit NuoF (07815) (Supplementary Data 3 and 4). This very low ~2% overlap (6 genes from 352) at gene-level is consistent with the near lack of agreement between highly ranking gene sets grouped based on q-values or CONSENSUS ranks from differential transcriptional and translational analysis, respectively (Supplementary Fig. 6). If we define transcriptional and translational regulation being coupled when a gene shows homodirectional expression changes as a DTR and DTL, our data

https://doi.org/10.1038/s41467-026-75309-w

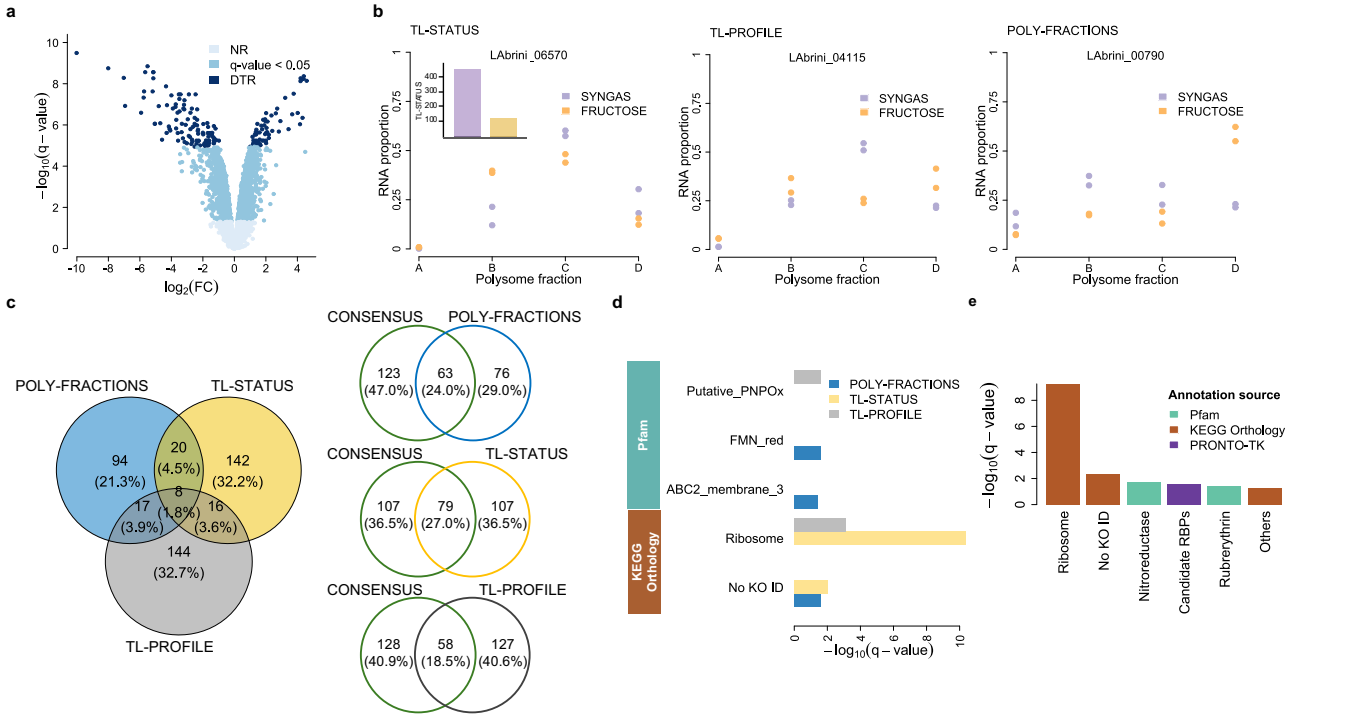

Fig. 2 | Limited transcriptional and translational control of autotrophy in *C. autoethanogenum*. **a** Volcano plot showing genes determined as differentially transcribed (DTR; #176) as a subset of 1784 genes with statistically different expression (q-value < 0.05) between syngas and fructose chemostats (DTRs are top 5% ranked according to q-value). NR not differentially regulated, FC fold-change. **b** Representative polysome profiles of top-ranking genes for each of the three metrics display the mRNA proportions of a gene across the ribosome-free fraction (A) and the polysome-bound fractions B (monosome), C (low ribosome density), and D (high ribosome density). Data are average ± standard deviation between biological duplicate chemostat cultures. For the TL-STATUS metric, inset shows the calculated translation status (i.e., ratio between the sum of the mRNA proportions quantified in the ribosome-bound and ribosome-free fractions). Bars are aggregate of merged data from $n = 2$ independent chemostat cultures. **c** Three-set Venn diagram showing the overlaps between the differentially translated genes (DTL) identified by the POLY-FRACTIONS, TL-STATUS, and TL-PROFILE metrics. The two-set Venn diagrams show the overlap between the DTL identified by the CONSENSUS approach and each of the three metrics. **d** Functional classes enriched in DTLs according to each metric by one-sided hypergeometric test (FDR = 5%). Pfam, Pfam entries[56] from eggNOG-mapper 2.1.12[143]; KEGG Orthology, KEGG Orthology (KO) functional categories[55] from Valgepea et al. (Level 3 in Table S4[13]); NS not significant. **e** Functional classes enriched in DTLs according to CONSENSUS approach by one-sided hypergeometric test (FDR = 5%). PRONTO-TK, computationally predicted RNA-binding proteins by PRONTO-TK[45]. Source data are provided as a Source data file.

suggest that transcriptional and translational regulation involved in realizing autotrophy in *C. autoethanogenum* are uncoupled.

Consistent with analysis above, no enriched functional classes are shared between DTRs and DTLs (Fig. 3b). Furthermore, the enrichment data show that two key metabolic modules for autotrophy—KO functional categories "Acetate and ethanol production" and "Energy conservation"—are only regulated at transcript level while ribosomal proteins are only regulated at translational level (Fig. 3b). The former includes various alcohol and aldehyde dehydrogenases (including Adh4 [09125], the most abundant Adh enzyme in *C. autoethanogenum*)[13], the bifunctional AdhE1 (18700), and the aldehyde Fd oxidoreductase AOR2 (00495). Transcriptional regulation of these genes was also seen with faster autotrophic growth of *C. autoethanogenum*[34]. Additionally, strictly transcriptional regulation was used to up-regulate components of the Rnf complex (16135–16155), that generates the proton motive force to drive the ATPase in *C. autoethanogenum*[58,59] (see also Fig. 6). Transcripts of the Rnf complex are also up-regulated in *C. autoethanogenum* syngas vs fructose batch cultures[50]. Interestingly, among the translationally regulated ribosomal proteins, S7 (09680) is known to act as an autogenous translation repressor[60] while L35 (06570) can act in an extra-ribosomal context to inhibit ornithine decarboxylases[61], which support acid-resistance and maintenance of optimal growth in Clostridia[62]. Additionally, L7Ae (09690) participates in tRNA processing, RNA modification, and translational regulation in archaea[63]. Only four genes showed discordant changes between transcriptional and translational regulation, with LABRINI_07435 and LABRINI_00130 putatively involved in iron metabolism[64,65] (Supplementary Data 3 and 4). Discordant changes could potentially result from condition-specific regulation of translational efficiency, particularly to maintain stable iron metabolism, as the iron composition of the medium remains unchanged between the two conditions. Overall, our DTR and DTL dataset aligns with the general regulatory understanding that mostly transcription controls condition-specific responses while translation fine-tunes expression of proteins required across conditions. Certainly, regulatory strategies can be different at gene-level and can also change globally under specific growth conditions.

Mapping genome-wide transcriptional architecture

Experimental mapping of transcriptional architecture is essential to accurately identify key RNA sequences—5′UTR and 3′UTR—through which RBPs typically facilitate post-transcriptional regulation[43,44]. We determined 5′UTRs through identification of transcription initiation sites (TISs) using Cappable-seq[66] as it simplifies data generation and analysis, and improves reproducibility and robustness[66,67] over the widely used alternative method dRNA-seq[68] (Fig. 1). We identified 3′UTRs by mapping transcription 3′ ends (T3Es) using Term-seq[69] that has an advantage of ensuring that the sequences adjacent to adapters in the sequencing reads represent RNA 3′ termini originally present in the samples. Sequencing metrics and read statistics with mappings are in Supplementary Data 5. To accurately map TISs and T3Es as primary or internal sites at the level of transcriptional units[70], we organized *C.*

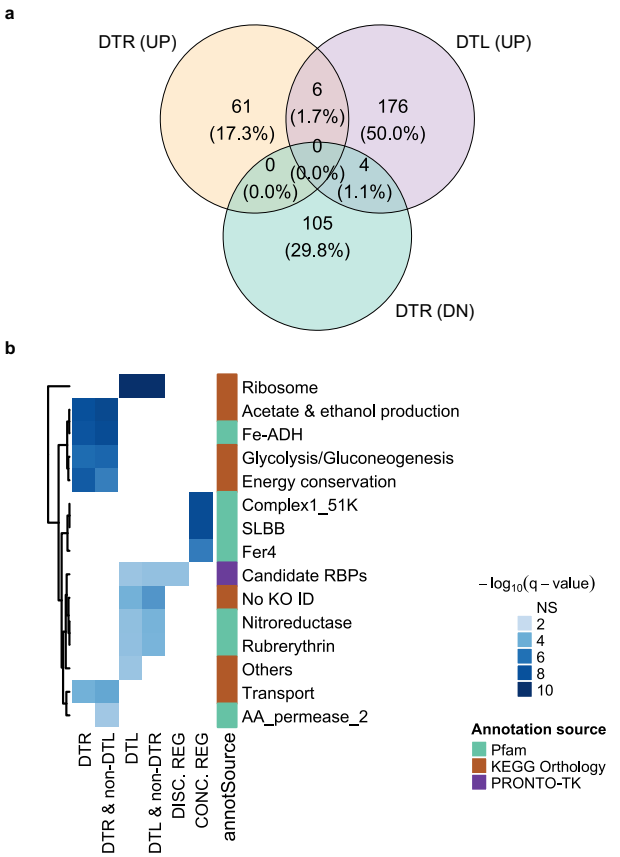

Fig. 3 | Uncoupled transcriptional and translational control for autotrophy of *C. autoethanogenum*. **a** Venn diagram showing overlaps between up- or down-regulated differentially transcribed genes (DTR) and differentially translated genes (DTL) between syngas and fructose chemostats. **b** Functional classes enriched in DTRs, DTLs, in genes exclusively regulated at transcriptional (DTR & non-DTL) or translational (DTL and non-DTR) level, and in genes which were both DTRs and DTLs showing concordant or discordant changes by one-sided hypergeometric test (FDR = 5%). DISC. discordant, CONC. concordant, Pfam, Pfam entries[56] from eggNOG-mapper 2.1.12[143], KEGG Orthology, KEGG Orthology (KO) functional categories[55] from Valgepea et al. (Level 3 in Table 43[13]), NS not significant. PRONTO-TK, computationally predicted RNA-binding proteins by PRONTO-TK[45]. Source data are provided as a Source data file.

autoethanogenum protein-coding genes into monocistronic operons with a single gene and polycistronic operons operationally defined as sets of protein-coding genes consecutively encoded on the same strand and separated by ≤60 nt. We identified 1721 single genes while 2221 genes were organized into 781 polycistronic operons (Supplementary Data 6).

We next employed a rigorous and heuristic multi-step procedure to determine TISs and T3Es for each operon (Fig. 4; see Methods for details). Shortly, we first extracted candidate sites upstream and downstream of an operon by removing sites with close-to-background read coverage and then used a series of established criteria—distance from CDS (filter #1 on Fig. 4), site coverage (#1), consistency of read coverage for TISs (#2), and uniformity of read coverage across the CDS (#3)—for filtering candidate sites (and clustering if needed; #4) to assign a single primary or multiple (primary and alternative) TISs and T3Es.

Analysis of Cappable-seq data identified 1179 unique TISs corresponding to 1588 genes (743 monocistronic and 300 polycistronic operons) that accounts for ~40% of protein-coding genes in *C. autoethanogenum* (Supplementary Data 7). From these, 1003 were identified from syngas and 991 from fructose with 815 from both cultures. In total, around 88% of TISs are primary and ~97% map to 5′ UTRs (Fig. 5a) while ~90% of genes were assigned with a single TIS (Fig. 5b). Our results show a median 5′UTR length of 54 nt with 75% being <100 nt (Fig. 5c and Supplementary Fig. 7a), similar to values seen for *C. autoethanogenum* batch cultures using dRNA-seq[71]. We took advantage of the experimental TIS data for promoter motif identification using MEME[72] for primary TISs. This supported the quality of our TIS data as we detected the well-described Pribnow box (TATAAT)[73] motif 10 nucleotides upstream of TISs for ~74% of TISs and, at a lesser extent, the −35 motif (TTGTCA) for ~8% of TISs (Fig. 5d). Notably, the TG dinucleotide in the Pribnow box[74,75] and the AT-rich region downstream of the −35 motif[76] stimulate transcription.

Analysis of Term-Seq data identified 751 unique TE3s, 620 from syngas and 621 from fructose with 490 from both cultures, for a total of 765 genes (Supplementary Data 7). Overall, ~70% of T3Es are primary (Fig. 5a), ~71% of genes were assigned with a single T3E (~23% with two) (Fig. 5b), and the median 3′UTR length was 122 nt with 75% being <241 nt (Fig. 5c; Supplementary Fig. 7b). Interestingly, ~21% of T3Es mapped to CDSs (Fig. 5a), indicating potentially premature termination or processing[77], that was dependent on the growth substrate for 46 monocistronic and 15 polycistronic operons functional in transcription, chemotaxis, transport, amino acid metabolism, and glycolysis/gluconeogenesis (Supplementary Data 8). We note that, to the best of our knowledge, determination of T3Es has been performed only twice before for acetogens[78,79].

We show the localization of TISs and T3Es for genes in key pathways for autotrophy in Fig. 6. More broadly, Supplementary Data 9 contains coordinates and annotations of CDSs, TISs, and T3Es to allow intuitive exploration of *C. autoethanogenum* transcript boundaries by any visualization tool, for instance with the open-source Integrative Genomics Viewer (IGV)[80].

Differential usage of TISs and T3Es for autotrophy and heterotrophy

To explore the extent of differential usage of TISs and T3Es between autotrophy and heterotrophy, we next classified genes according to the growth substrate specificity of their TISs and T3Es. The large majority of genes (~89%) feature a single TIS used for both syngas and fructose (Fig. 5e; light blue) while only a ~6% minority of genes use TISs exclusive to syngas (~3%; green) or fructose (~3%; orange), which includes a transcription elongation factor (07115) (Supplementary Data 10). The remaining set of genes show a composite profile of TIS usage with both TISs exclusive and common for either substrate. Similarly to TIS data, most genes (~75%) feature a single T3E for both syngas and fructose (Fig. 5e; light blue) (Supplementary Data 11). However, RNA processing at 3′UTRs appears to be more dependent on growth substrates as ~12% of genes show T3Es exclusive to fructose (Fig. 5e; orange) with another ~7% which show exclusive T3Es for fructose along with shared T3Es (light gray). Interestingly, a glyceraldehyde-3-phosphate dehydrogenase (08720) with an accompanying transcriptional regulator (08725) showed the most versatile T3E usage with both T3Es exclusive and common for either substrate (Fig. 5e; gray). Notably, we did not detect a single gene showing only T3Es exclusive for syngas.

Importantly, we detected enrichment of genes involved in energy conservation in the group of genes featuring syngas-specific TISs in addition to TISs shared for both substrates (Fig. 5f). This includes genes encoding the Rnf complex, a key activity for autotrophy in acetogens[58,59] (Fig. 6). Furthermore, genes with syngas-only TISs include several genes with Pfam domains involved in two-component signal transduction systems (TCS). These genes encode for transcriptional regulators (domain "Trans_reg_C"), histidine kinases (HK; "HisKA"), and response regulator (RR; 'Response_reg')

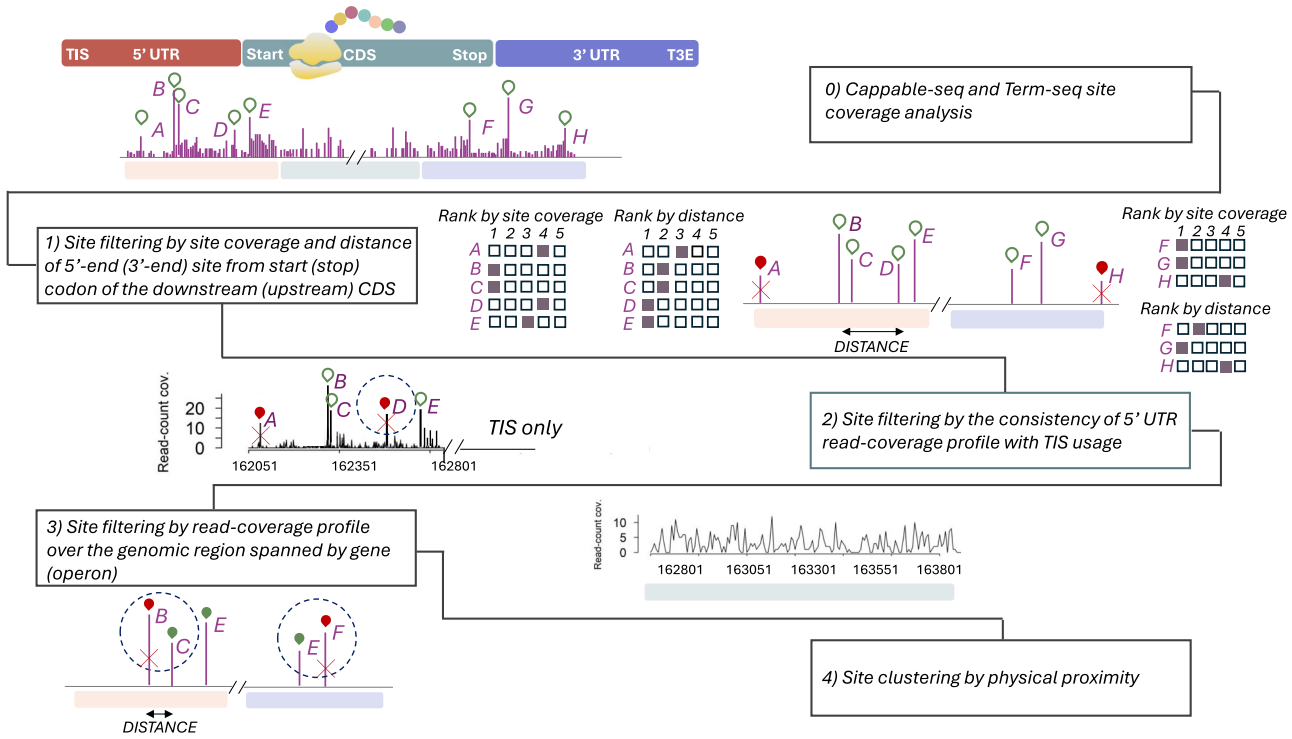

Fig. 4 | Heuristic procedure used in this work for genome-wide identification of transcription initiation (TIS) and transcription 3′ end (T3E) sites. The procedure consists of multiple filtering steps to ensure reliable identification of TISs and T3Es from preliminary sites extracted from Cappable-seq and Term-seq analysis (see Methods for details). Shortly: Filter (1) selects preliminary sites based on two criteria: site coverage in read counts and distance from the start (stop) codon of the downstream (upstream) coding DNA sequence (CDS). Sites are partitioned into five quantiles according to each criterion and quantiles for each TIS or T3E are combined. A TIS (T3E) passes to next step if the composite quantile accounting for both criteria is sufficiently high; Filter (2) is exclusively applied to 5′-untranslated regions (UTRs) and checks if it contains a stretch of sequence with a length of ≥50% of the total UTR length with a median read coverage ≥5 and ≥50% higher than for 100 nt upstream of the TIS; Filter (3) assesses the genomic region spanned by the gene (operon) for uniformity in read coverage; Filter (4) selects the TIS (T3E) closest to the start (stop) codon of the downstream (upstream) CDS for genes with multiple TISs or T3Es that are closer than 5 nt from each other.

proteins. Interestingly, we previously isolated *C. autoethanogenum* strains with improved phenotypes from autotrophic adaptive laboratory evolution carrying mutations in HKs and RRs[36], which might be part of yet-to-be-described regulatory networks[81]. Indeed, autophosphorylation of a HK by signal sensing drives the phosphorylation and activation of a RR to regulate diverse adaptive responses[82,83]. Notably, LABRINI_04855 harbors the ligand-binding domains GAF[84] and PAS[85], which can bind carbon monoxide[86], and the HK-A domain, which is the phospho-acceptor domain of HKs. Furthermore, the two adjacent genes− LABRINI_04850 and LABRINI_04860−contain the REC domain[82], which receives the signal from an HK. An additional TCS was enriched here with LABRINI_16335 containing a REC domain and LABRINI_16340 containing the HK-A domain. These syngas-only TISs could potentially be controlled by the σ^{54}-dependent Fis family transcriptional regulator (02225) since it also has a syngas-only TIS and a σ^{54} interaction domain occurs repeatedly in TCS genes[87,88].

Only two genes displayed both a syngas-specific and a fructose-specific TIS: the radical SAM protein (11570) and a transcription elongation factor (07115), the latter being consistent with the identification of transcriptional regulators (02225, 12490, 13845, 02980, 18605, 18630) which are associated with substrate-specific TISs. Notably, genes featuring exclusively fructose-specific T3Es were enriched with TCSs, some of which include genes encoding HAMP-domain containing HKs (12620-12625, 03770-03775), which are putatively involved in the coordination of cell wall remodeling during cell division in Gram-positive bacteria[89,90]. For T3Es, the KO functional category "Acetate and ethanol production" was enriched in genes displaying TE3s specific to either syngas or fructose (Fig. 5f), indicating the potential relevance of regulation of termination in expression of genes involved in product synthesis.

Transcription-initiation signals for the Rnf complex are enhanced for autotrophy

Our analysis detected TISs and T3Es for genes in key metabolic pathways and activities for autotrophic growth of *C. autoethanogenum*: acetate and ethanol production, energy conservation, the WLP, and hydrogenases (Fig. 6). Comparison of the strength of transcription-initiation and termination signals between the two substrates could reveal regulation critical for autotrophy.

Among the TISs identified in both syngas and fructose, we detected significant differences ($q < 0.05$) in the expression levels (i.e., site coverages) of 155 TISs linked to 144 genes between the two substrates (Supplementary Data 7). Importantly, changes in transcription-initiation signals are consistent both in directionality and magnitude with differential expression of respective transcripts (Supplementary Fig. 9). Genes with up-regulated or down-regulated TISs were enriched within the top or bottom ranks of genes ordered by transcript expression changes, respectively (see Methods for details; Supplementary Fig. 9a). Changes in TIS signals and transcript expression both correlate and match quantitively well (Supplementary Fig. 9b). Strikingly, transcription-initiation signals for components of the Rnf complex, which plays a key role in energy conservation for autotrophy[59,91,92], were strongly enhanced on syngas vs fructose (Fig. 6 and Supplementary Fig. 10a). Thus, the stronger initiation signals plus syngas-specific TISs (Fig. 5f) most likely lead to the enhanced expression of the Rnf complex CDS transcripts (Fig. 3B and Supplementary Data 3). Interestingly, genes with weaker initiation signals on syngas

https://doi.org/10.1038/s41467-026-75309-w

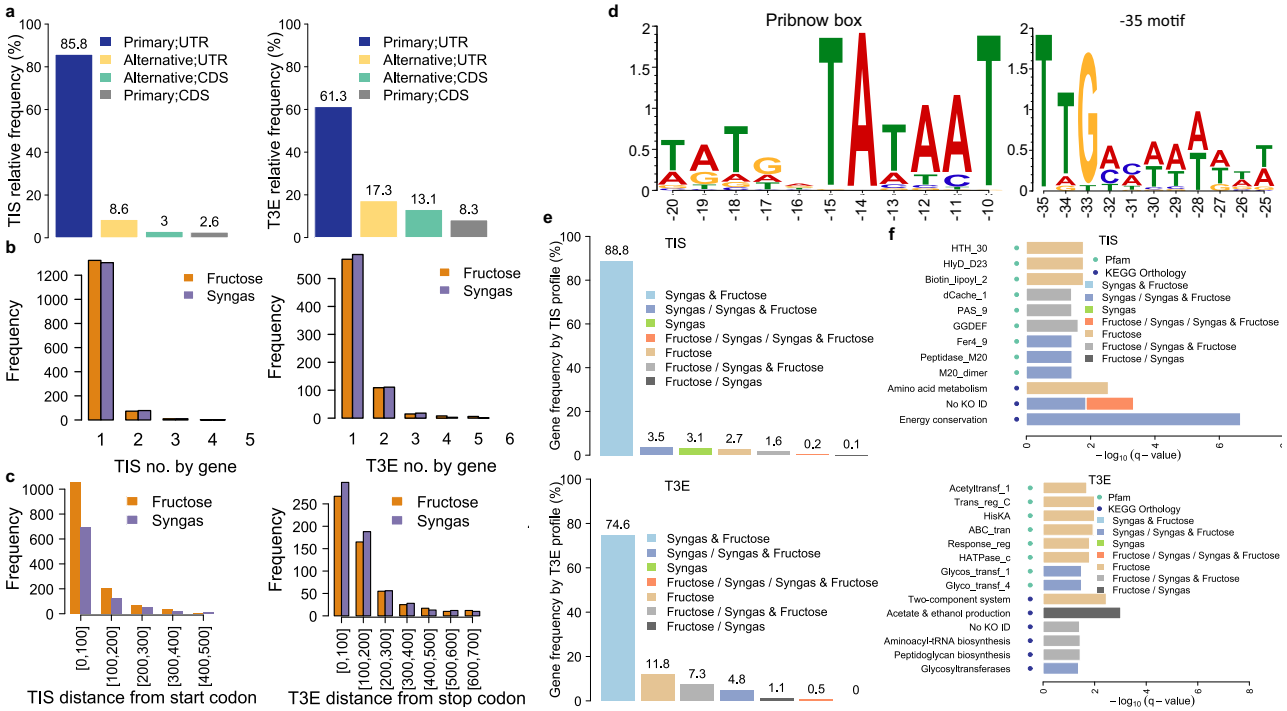

Fig. 5 | Characteristics of transcriptional architecture in *C. autoethanogenum*. **a** Classification of transcription initiation (TIS) and transcription 3′ end (T3E) sites according to strength (primary or alternative) and localization (UTR or coding DNA sequence, CDS). Primary site shows highest site coverage and shortest distance from CDS start (stop) codon while remaining sites passing the filtering procedure shown on Fig. 4 are identified as alternative sites. **b** Frequency of TISs and T3Es per gene for syngas and fructose chemostats. **c** Distribution of 5′ and 3′UTR lengths for syngas and fructose chemostats (5′UTR < 500 nt; 3′UTR < 700 nt; see Supplementary Fig. 7 for full distribution). **d** Promoter motifs identified in 5′UTRs by MEME[72]. **e** Frequency of gene-specific TIS or T3E profiles for syngas and fructose chemostats. Bars are aggregate of merged data from $n = 3$ independent chemostat cultures. Syngas & Fructose, site(s) shared between two conditions; Syngas/Syngas & Fructose, site(s) unique to syngas and site(s) shared between two conditions; Syngas, site(s) unique to syngas; Fructose, site(s) unique to fructose; Fructose/Syngas & Fructose, site(s) unique to fructose and site(s) shared between two conditions; Fructose/Syngas/Syngas & Fructose, site(s) unique to syngas, site(s) unique to fructose, and site(s) shared between two conditions; Fructose/Syngas, site(s) unique to syngas and site(s) unique to syngas. See Supplementary Fig. 8 for a visual schematic of the different profiles. **f** Functional classes enriched in genes defined by TIS and T3E profile by one-sided hypergeometric test (FDR = 5%). Pfam, Pfam[56] entries from eggNOG-mapper 2.1.12[143]; KEGG Orthology, KEGG Orthology (KO) functional categories[55] from Valgepea et al. (Level 3 in Table S4[13]). Source data are provided as a Source data file.

were enriched with CooS1 carbon monoxide dehydrogenase subunits (15005–15015), genes involved in ethanol production (02655, 16430, 18700, and 19700), genes belonging to glycolysis/gluconeogenesis, and numerous transcription factors (Fig. 6 and Supplementary Fig. 10a). Within the T3Es detected in both syngas and fructose, we measured significant differences in the expression levels of 439 T3Es linked to 341 genes between the two substrates (Supplementary Data 12). Genes with enhanced termination signals for autotrophy included a gene cluster for cobalamin biosynthesis (05425–05445) while genes with repressed termination signals were enriched with ABC transporters, flagellar proteins, and genes involved in cell wall metabolism (Supplementary Fig. 10b). The relevance of these changes in termination signal strengths for autotrophy remain unclear.

RNA-binding proteins (RBPs) involved in transcriptional and translational regulation of mRNAs for autotrophy

Accurate mapping of transcriptional architecture defines UTR RNA sequences where RBPs could bind to execute post-transcriptional regulation. We could identify 5′UTRs for ~66% of DTRs and ~61% of DTLs, and 3′UTRs for ~28% of DTRs and ~10% of DTLs. To identify potential RBP binding regions in UTRs and thus RBP-RNA interactions, we first predicted potential RBPs for *C. autoethanogenum* using PRONTO-TK[45] (Fig. 1 and Supplementary Data 13), a neural network-based protein function prediction tool that uses ProtT5-XL protein language model embeddings to encode sequence-derived biochemical and structural features (see Methods for details). We trained a binary classifier using the "RNA binding" GO term and its descendants, based on experimentally validated protein annotations from the UniProt knowledgebase[93]. We used a conservative posterior probability threshold of 0.75 which retained 100 RBPs. This threshold was chosen to minimize false positives while accepting that some genuine RBPs with weaker sequence signatures might be missed. We then used the computational tool catRAPID[46] to search for candidate RBP binding sites in the UTRs of DTRs and DTLs (Fig. 1; Supplementary Data 14), while excluding structural ribosomal proteins from the RBP list (see Methods for details). We prioritized high-confidence predictions by retaining interactions ranking in the top 25% of catRAPID scores, which could potentially exclude weaker but functionally relevant interactions. Overall, RBP binding sites were predicted for 69 differentially regulated genes: in 5′UTRs of ~11% of DTRs (20 genes) and ~15% of DTLs (27 genes), and in 3′UTRs of 12% of DTRs (21) and ~5% of DTLs (11) (Fig. 7 and Supplementary Data 14). Most RBP target genes were regulated exclusively transcriptionally (37 out of which 18 up-regulated and 19 down-regulated on syngas vs fructose) or translationally (35 up-regulated) (Fig. 7). The remaining three RBP targets were a ferritin-encoding gene (00130) showing different regulation between transcription and translation, and a heat-shock protein (10470) and a ketol-acid reductoisomerase (00585) showing concordant regulation. Interestingly, 00585 is among the top 10 most abundant proteins in *C. autoethanogenum*[13]. Most RBPs recognized cis-regulatory elements in both 5′ and 3′UTRs of target genes while individual genes were rarely bound by RBPs in both of their UTRs. Within the latter, a potentially

https://doi.org/10.1038/s41467-026-75309-w

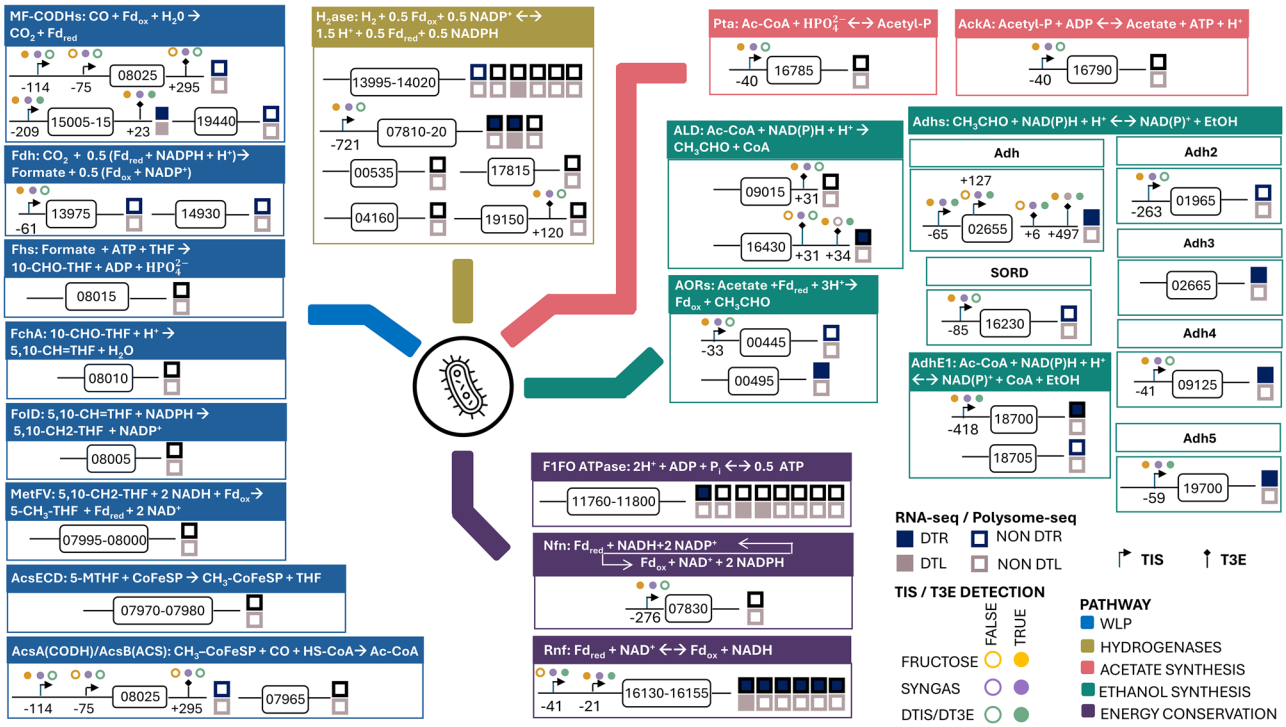

Fig. 6 | Transcriptional architecture and transcriptional/translational regulation in key metabolic pathways for autotrophy of *C. autoethanogenum*. Boxed numbers are LAbrini gene IDs. Transcription initiation (TIS) or transcription 3′ end (T3E) site distance shown from start codon of downstream coding DNA sequence (CDS) or stop codon of upstream CDS, respectively. Color-coding of circles: open yellow or purple, TIS/T3E not detected for fructose or syngas; filled yellow or purple, TIS/T3E detected for fructose or syngas; open green, not differentially expressed TIS or T3E; filled green, differentially expressed TIS (DTIS) or T3E (DT3E). Color-coding of squares: filled blue, differentially transcribed gene (DTR); open blue, non-differentially transcribed gene (NON DTR); filled gray, differentially translated gene (DTL); open gray, non-differentially translated gene (NON DTL). MF-CODH monofunctional carbon monoxide dehydrogenase, Fd ferredoxin, THF tetrahydrofolate, 10-CHO-THF 10-formyl-THF, 5,10-CH=THF 10-methenyl-THF, 5,10-CH2-THF 10-methylene-THF, 5-CH_3-TFH 5-methyl-THF, CoFeSP corrinoid iron sulfur protein, Ac-CoA acetyl-CoA, EtOH ethanol, SORD zinc-dependent dehydrogenase. See Supplementary Data 1 for all gene descriptions. Bacteria icon designed by Good Ware from Flaticon (www.flaticon.com).

relevant example for autotrophy is the alcohol dehydrogenase 02655. While genes involved in coenzyme synthesis for redox reactions, quorum sensing, and base excision repair were regulated by RBPs exclusively via 3′UTRs, translation-related genes (e.g., amino acid metabolism, tRNA processing) and transporters showed binding events in both UTRs.

The above-mentioned UTRs showed binding sites for 14 RBPs while none were found to bind uniquely either to 5′UTRs or 3′UTRs (Fig. 7). Furthermore, none of the 69 target genes were linked to regulation by a single RBP. Notably, one RBP was translationally upregulated on syngas: the polynucleotide phosphorylase PNPase (17015) involved in mRNA turnover[94] and RNA-mediated regulation[95]. The remaining RBPs included proteins well-known for their roles in RNA metabolism: two RNA methyltransferases (MTases) (12395, 06560)[96]; the ribonucleases (RNases) Y (17055), III (16815), HII (16885), and M5 (11465) involved in RNA decay[97–99]; the Mini RNase III (09770), which can realize sequence-specific cleavage of dsRNAs[100]; the transcription attenuation protein NusA (16970)[101,102]; two DEAD/DEAH box helicases (07100 and 15020) involved in RNA decay[103]; and two genes (14195, 19185) encoding a RluA family pseudouridine synthase, which is the major mRNA pseudouridine synthase in *E. coli*[104].

None of the RBPs were predicted to bind to genes involved in the following key activities for autotrophy of acetogens: C_1-fixation using the WLP, energy conservation through the Rnf complex, redox homeostasis through the Nfn transhydrogenase, or the various hydrogenases. At the same time, multiple RBPs showed UTR interactions with three alcohol dehydrogenases (08985, 08625, and 02655) (Fig. 6) that can be critical for maintenance of redox and energy homeostasis for *C. autoethanogenum* autotrophy through regulation of carbon flux between acetate and ethanol[14,105], the two major metabolic products (Supplementary Fig. 1). Several RBPs targeted translation-related processes, including ribosomal structural proteins (30S ribosomal proteins S10 and S12 encoded by 09665, 09685), tRNA synthetases (06555, 06580, 06690), genes involved in amino acid metabolism (03730), and in biosynthesis of tRNA hypermodified nucleosides (06250), namely queuosine and N^6-threonylcarbamoyladenosine, which are essential for modulating protein synthesis[106] (Fig. 7). Relevant to autotrophic biomass formation through gluconeogenesis was the binding of several RBPs to the 3′UTR of the type I glyceraldehyde-3-phosphate dehydrogenase (08720).

Discussion

While post-transcriptional regulation of gene expression plays an important role in acetogens[19], none of the key players in this regulatory layer—RBPs—had been described before. We thus also lacked knowledge about RBP-RNA interactions in acetogens that could facilitate global adjustments in metabolism, for instance towards autotrophy. To address these gaps with this work, we employed a comprehensive approach by combining chemostat cultures, functional genomics, and computational methods to predict genome-wide RBPs and RBP-RNA interactions in the model-acetogen *C. autoethanogenum*.

We focused our approach on genes displaying transcriptional and/or translational regulation by their transcripts being differentially transcribed and/or translated during autotrophy vs heterotrophy. Widespread translational regulation in general could imply its dominant role in regulating protein levels towards realizing a cell phenotype. We determined a low number of DTLs (186) that is consistent with the good correlation (R ~ 0.69 for 1797 genes) between

https://doi.org/10.1038/s41467-026-75309-w

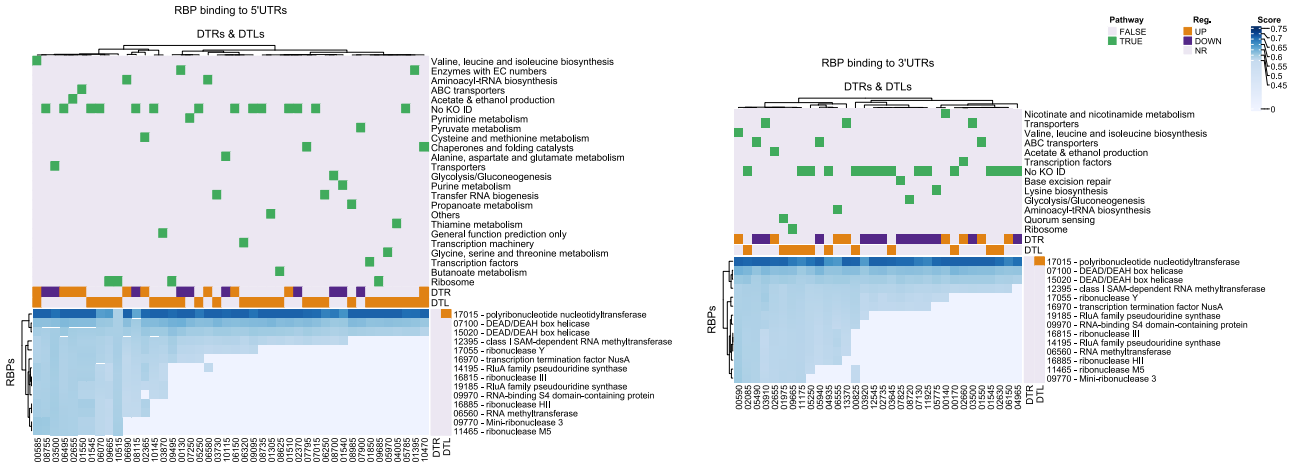

Fig. 7 | RNA-binding proteins (RBPs) linked to differentially regulated genes in *C. autoethanogenum*. Predicted RBP interactions with 5′ and 3′UTRs of differentially transcribed genes (DTRs) and differentially translated genes (DTLs) with RBPs in rows and target genes in columns. Blue heatmap shows catRAPID scores for RBP-RNA interactions. Row dendrogram on the left side and column dendrogram on the top of the heatmaps are from complete-linkage hierarchical clustering of the Euclidean distance matrix based on RBP-RNA interaction scores computed by catRAPID. KEGG Orthology functional categories[55] from Valgepea et al. (Level 3 in Table S4)[13] for target genes are shown on top. See Supplementary Data 1 for target gene descriptions. Source data are provided as a Source data file.

transcript levels quantified in syngas chemostats here and protein levels in LAbrini syngas chemostats in previous works[35,81] (Supplementary Fig. 11). The low DTL count is also in line with the low number of proteins differentially expressed between CO, CO + H_2, and CO + CO_2 + H_2 grown *C. autoethanogenum* chemostats[107]. Indeed, metabolic flux adjustments between the latter cultures are dominantly accompanied by changing enzyme catalytic rates rather than concentrations[13]. Such post-translational regulation of fluxes is also seen in self-oscillating *C. autoethanogenum* autotrophic cultures[12,14] and this is presumably the most efficient regulatory mode of fluxes for energy-limited metabolism since close to half of ATP for biomass proliferation is used for protein synthesis[108,109]. Furthermore, keeping a higher baseline expression of key proteins would allow cells to use post-translational regulation for a more rapid reaction to gaseous substrates when these become available in natural environments. At the same time, nearly half of transcripts showed statistically different expression (q-value < 0.05) here (Fig. 2a and Supplementary Data 3), consistent with data from *C. autoethanogenum* syngas and fructose batch cultures[50]. Hence, transcriptional regulation seems to be required to ensure the baseline proteome expression for both autotrophy and heterotrophy. Our data thus suggest that *C. autoethanogenum* does not rely on strong or on/off regulation of genes key for facilitating stable growth on gas and sugar. This is in line with conclusions drawn in a recent review about different layers of regulation of metabolism in acetogens[3]. Still, transcriptional control of Rnf complex components and alcohol and aldehyde dehydrogenases detected in our work (Fig. 6) suggests attractive strain engineering targets in key metabolic activities of *C. autoethanogenum*.

Overall, ~19% of differentially regulated genes showed interactions with RBPs in our dataset (Fig. 7). The fact that we did not identify any RBPs binding only to genes with key activities for autotrophy (e.g., WLP, Rnf, Nfn, hydrogenases) implies that acetogens, at least *C. autoethanogenum*, do not seem to use an RBP-level mechanism for specifically regulating expression of genes exclusively needed for autotrophy. Thus, further studies are needed to understand the mechanisms behind post-transcriptional regulation of gene expression in acetogens[19]. Although multiple RBPs targeted alcohol dehydrogenases, potentially critical for maintenance of redox and energy homeostasis[14,105], elucidation of key RBPs regulating alcohol dehydrogenases, however, would be highly challenging due to the large number of candidate RBPs, their binding to other target genes with potentially essential functions, and the difficulties with creating such a number of *C. autoethanogenum* gene deletion mutants. Importantly, our study predicted several RBP-RNA interactions well-known in bacteria that are needed for optimal growth in general. These interactions are therefore also involved in mediating differential gene transcription and translation profiles between autotrophy and heterotrophy in *C. autoethanogenum* and will be thus discussed in more detail next.

Several differentially regulated genes in our dataset showed binding by the RBP NusA (Fig. 7; 16970), a factor for transcription attenuation: a process where bacteria direct the RNA polymerase to either terminate transcription or transcribe downstream genes in an operon as a response to metabolic signals[101,102]. In contrast to translation-controlled termination of transcription in *E. coli*, the Gram-positive model microbe *Bacillus subtilis* (*C. autoethanogenum* is Gram-positive) lacks kinetic coupling between the transcription elongation factor and the pioneering ribosome[110]. Therefore, operon-specific RBPs[111–114] or trans-acting factors, such as NusA[77,115], are expected to support transcription attenuation. Our study predicts NusA involvement in realizing autotrophy in *C. autoethanogenum*, as it is predicted to bind to genes involved in metabolic processes that are sensitive to transcriptional attenuation such as biosynthesis of thiamine, amino acids, tRNA synthetases, and ribosome biogenesis[116]. Transcription termination is often triggered by the arrangement of one of the two mutually exclusive stem structures in the nascent transcript, where the second stem is followed by a poly-U sequence forming a terminator and the second strand of the first stem base-pairs with the first strand of the second stem[117]. Indeed, we detected the presence of this characteristic arrangement in the 5′UTR of three genes targeted by NusA in our study using PASIFIC[118]: 06495, 01550, and 02365 encoding a tyrosine-tRNA ligase, a transmembrane protein, and a homoserine O-succinyltransferase, respectively. A recent study suggests that NusA-mediated stabilization of transcriptional pausing and attenuation could be involved in the establishment of transcription-translation coupling through the interaction between NusA and translation initiation factor IF2[119]. This mechanism is unlikely in *C. autoethanogenum* as *B. subtilis* lacks coupling between transcription and translation[110]. Thus, further studies are required to elucidate the role of NusA in *C. autoethanogenum*. Our results further show binding of an array of RNases to differentially regulated genes (Fig. 7). RNases are essential mediators in RNA maturation, quality control, and degradation where changes in tRNA and rRNA maturation impact translational

regulation while changes in mRNA stability affect transcript levels. mRNA decay in Gram-positive bacteria relies on the cooperation between endoribonucleases, which cleave mRNAs and provide access to 5′ and 3′ extremities, and 5′ → 3′ and 3′ → 5′ exoribonucleases, which degrade the cleaved RNA fragments[26,120]. Our data for *C. autoethanogenum* is consistent with this model as we predicted binding of both endoribonucleases (RNase Y, 17055; RNase III, 16815; and RNase M5, 11465; Mini RNase III, 09770) and exoribonucleases (PNPase, 17015 and RNase HII, 16885).

The highest number of target genes was detected for RNase Y, the major decay-initiating endonuclease in *B. subtilis* and many Firmicutes[99,121]. For RNase Y target selection, supporting proteins are proposed to be important in the Gram-positive *Staphylococcus aureus*[122]. This is because RNase Y appears to be strongly influenced by features distal to the position of cleavage, possibly facilitated by RNA secondary structure and RNA-protein interactions[123]. Our study suggests that this could be the case for *C. autoethanogenum* as well since RNase Y target genes were bound also by RNA helicases and RNA methyltransferases (Fig. 7 and Supplementary Data 14). Interestingly, while RNase M5 in *B. subtilis* is thought to be almost exclusively active in 5S rRNA processing[124], we predicted its binding to an alcohol dehydrogenase, multiple transporters, S6 and S10 ribosomal proteins, and genes in folate and thiamine metabolism (Fig. 7 and Supplementary Data 14). Notably, ~88% of RNase M5 targets were also targeted by RNase III and Mini RNase III. While RNase III was initially assigned a secondary role in *B. subtilis*[125], it has now been shown to be important in *B. subtilis* for post-transcriptional catalytic and binding activities[98] and to be involved in translational regulation in *S. aureus*[126]. Thus, it is likely that all four described endoribonucleases contribute towards autotrophy in *C. autoethanogenum*. For degradation of the cleaved RNA, *C. autoethanogenum* seems to primarily rely on the exoribonuclease PNPase as it targeted all the differentially regulated genes that the four endoribonucleases targeted (Fig. 7). What is more, PNPase was translationally up-regulated on syngas (Fig. 7). Use of the phosphorolytic enzyme PNPase could be beneficial for an energy-limited metabolism as the PNPase degradation products nucleoside diphosphates conserve energy[26]. Interestingly, PNPase can also play a role in complex cell adaptive responses through its recruitment in different multiprotein complexes[94]. RNA degradation could also involve the poorly characterized exoribonuclease RNase HII as it shared an unexpectedly high fraction of targets in common with RNase Y (89%), RNase M5 (67%), and RNase III (90%).

In terms of post-transcriptional RNA modifications for differentially regulated genes, the RBP pseudouridine synthases (19185, 14195) could be relevant (Fig. 7) as pseudouridine is a ubiquitous bacterial RNA modification, primarily on tRNA and rRNA, and secondarily on mRNA[104]. Whereas the modification plays a role in mammalian transcript stabilization[127] and modulation of transcript translatability[128,129], its potential effects on mRNA function in bacteria are largely unexplored[130]. The fact that pseudouridine synthases targeted both DTRs and DTLs in our dataset suggests that pseudouridine can affect both transcription and translation in bacteria, similarly to mammals. Its scope seems wide as predicted pseudouridine synthase targets included an alcohol dehydrogenase, transporters, the threonine-tRNA ligase, and the 30S ribosomal protein S10, which is part of the processive rRNA transcription and antitermination complex.

Our in silico reconstruction of RBP-mediated regulatory interactions has limitations as it relies on two computational tools that both involve predictive uncertainties. For instance, PRONTO-TK predictions could be limited by the underlying training data that are biased towards well-studied organisms and could potentially miss RBPs with non-canonical binding domains or, more generally, yet-to-be-elucidated regulatory mechanisms in non-model organisms. In addition, the catRAPID sequence-based algorithm cannot fully account for the dynamic cellular environment, including competitive protein binding, RNA conformational changes, or post-translational modifications that influence RBP activity in vivo. Nevertheless, we employed several design choices to minimize computational artifacts. Firstly, conservative filtering was adopted to minimize false positives in predicted RBPs while accepting that some genuine RBPs could be missed. Secondly, the requirement for convergent evidence from multiple scoring metrics reduced the likelihood of spurious predictions of RBP-RNA interactions. Overall, our computational predictions should be interpreted as well-founded hypotheses that require future experimental validation.

We believe our work to be important for two reasons. Firstly, we provide a systems-level steady-state dataset for an acetogen comparing heterotrophic and autotrophic growth. Importantly, this combined description of transcriptome expression, polysome profiles, and transcriptional architecture advances fundamental understanding of gene function, gene expression regulation, and metabolism of the ancient metabolism of acetogens. Secondly, we report predicted genome-wide protein-RNA interactions for differentially regulated genes in a model-acetogen. This is important as it provides novel targets for metabolic engineering of acetogen cell factories from the unexplored space of RBPs. Future work will need to experimentally quantify the effects of genetic perturbations of candidate RBPs on acetogen autotrophy, including potentially synergistic or epistatic links between RBPs.

Methods

Bacterial strain and cultivation conditions

The *C. autoethanogenum* strain LAbrini[36] deposited in the German Collection of Microorganisms and Cell Cultures (DSM 115981) was used in this work.

C. autoethanogenum was grown in biological triplicate chemostat continuous cultures either autotrophically on syngas (50% CO, 20% H_2, 20% CO_2, and 10% Ar; AS Linde Gas) or heterotrophically on fructose (15 g/L) in a chemically defined medium (without yeast extract; Supplementary Methods). Cultures were operated under strictly anaerobic conditions at 37 °C and at pH 5 (maintained by 5 M NH_4OH) in 1.4 L Multifors bioreactors (Infors AG) at a working volume of ~750 mL connected to a Hiden HPR-20-QIC mass spectrometer (Hiden Analytical) for online off-gas analysis. Antifoam (435530; Sigma-Aldrich) was continuously added to the bioreactor at a rate of 10 µL/h to avoid foaming. We used a syngas flow rate of 50 mL/min and agitation of 675 RPM for autotrophic, and a N_2 flow rate of 50 mL/min and agitation of 200 RPM for heterotrophic cultures (CO_2, instead of N_2, was used for 20 h post-inoculation). With this, we achieved steady-state biomass concentrations of 1.37 ± 0.003 and 1.03 ± 0.008 g of cell dry weight per liter for syngas and fructose cultures, respectively, for chemostats at dilution rates (D) 1.03 ± 0.05 and 0.997 ± 0.003 day^{-1} for syngas and fructose cultures, respectively. Steady-state results and samples were collected after culture optical density (OD), gas uptake, and production rates had been stable for at least three working volumes.

Biomass concentration and extracellular metabolome analysis

Biomass concentration was calculated using culture OD and the correlation coefficient between culture OD and biomass concentration established at 0.23. Extracellular metabolome analysis of acetate, ethanol, and 2,3-butanediol from filtered culture broth samples (stored at –20 °C until analysis) was performed by HPLC (Shimadzu Prominence-I LC-2030 plus system) using a Rezex™ ROA-Organic Acids H^+ (8%) 300 × 7.8 mm column (00H-0138-K0; Phenomenex) and a guard column (03B-0138-K0; Phenomenex). Twenty microliters of the sample was eluted isocratically at 45 °C for 30 min with 0.5 mM H_2SO_4 at 0.6 mL/min. Identification and quantification was performed using relevant standards, a refractive index detector (RID-20A; Shimadzu), and the software LabSolution (Shimadzu). We note that cells produced 2 R,3R-butanediol.

Cappable-seq

C. autoethanogenum chemostat cultures were sampled for Cappable-seq by pelleting either 5 (syngas cultures) or 6.5 mL (fructose cultures) of culture broth (to match biomass amounts) by centrifugation (5000 × *g* for 3 min at 4 °C), discarding the supernatant, and flash-freezing in liquid N_2 followed by storage at –80 °C until analysis. Total RNA from frozen samples was extracted using the RNeasy Mini Kit (Qiagen) according to the manufacturer's instructions with in-column DNase treatment with the RNase-Free DNase Set (Qiagen). Total RNA samples were then converted to Cappable-seq libraries[66]. Following enrichment and decapping, RNA samples were converted to Illumina-ready libraries using the SMARTer smRNA-seq kit (TakaraBio). Library qualities were assessed by the Agilent 2100 Bioanalyzer and finally libraries were sequenced using the Illumina Novaseq 6000 sequencer with 1 × 100 bp cycles (single-end).

Term-seq

The same cell pellets as for Cappable-seq were used for Term-seq (see above for sampling details). Ribosomal RNA was depleted from total RNA using the RIBO-Zero kit (Illumina), following manufacturer instructions. Ribosomal RNA depleted-RNA 3′ ends were poly-adenylated, followed by RNA fragmentation, end-repair, and library preparation using the SMARTer smRNA-seq kit (TakaraBio). Library qualities were assessed by the Agilent 2100 Bioanalyzer and finally libraries were sequenced using the Illumina Novaseq 6000 sequencer with 2 × 100 bp cycles (paired-end).

Data analysis for genome-wide identification of TIS and T3E sites

Firstly, Term-seq reads (R1 or R2) were all trimmed of sequence elements added during library construction. Of each R1/R2 pair, trimmed-selected reads include either the R1 read, whenever the R1 contained the 3′ adapter (i.e., when the read reaches the end of the mRNA fragment), or the inverse-complement of the R2 read, which always includes the end of the mRNA fragment. Whenever possible, R1 was preferred over R2 because R1 generally has higher sequence quality. Trimmed Cappable-seq reads (by the position of their 5′-end) and trimmed-selected Term-seq reads (by 3′-terminal position) were mapped to the genome of *C. autoethanogenum* strain LAbrini (GenBank CP110420.1) using STAR[131]. Read quality control was carried out by Fastq and sequencing metrics and read statistics with mappings are in Supplementary Data 5.

Secondly, *C. autoethanogenum* CDSs were organized into monocistronic operons with a single gene and polycistronic operons operationally defined as sets of protein-coding genes consecutively encoded on the same strand and separated by ≤60 nt. For the analysis of Cappable-seq read coverage relative to operons, we implemented the following heuristic procedure:

1. For each operon, we considered genome regions comprising the location of the gene operon and its 5′ flanking (upstream) sequence up to the upstream gene operon on the same strand. Based on the genome annotation, we characterized each position within this region as hypothetical "5′UTR", coding region ("CDS"), or intergenic region ("IG") for polycistronic operons.
2. From the hypothetical "5′UTR" region, we identified the position *i* with maximum Cappable-seq 5′-end coverage: $C(Fructose)_i^M$, summing coverages of the three fructose bio-replicates with maximum coverage; $C(Syngas)_i^M$, summing coverages of the three syngas bio-replicates with maximum coverage.
3. We identified all positions *j* within "5′UTR", "CDS", or "IG" regions with coverages $C(Fructose)_j$ or $C(Syngas)_j$ such that $C(Fructose)_j \geq T \bullet C(Fructose)_i^M$ and $C(Syngas)_j \geq T \bullet C(Syngas)_i^M$, where $T = 0.1$ is a fractional threshold of the respective maximum coverages identified in the 5′UTR of the operon. We considered all sites identified in the "5′UTR" from fructose or syngas bio-replicates as potential TIS candidates, and all sites identified in "CDS" and "IG" regions as representing background coverages.
4. We characterized each site identified within the "5′UTR" region by its ranking relative to the coverages of those selected from "CDS" + "IG" regions for each operon ("*p*-value"). Thus, if 100 sites were identified as background in "CDS" + "IG" regions, a "5′UTR" site that had coverage higher than any of those coverages was assigned a *p*-value = 0.0. If, for instance, 10 sites from the "CDS" + "IG" region had higher coverage, it was assigned a *p*-value = 0.1 (10/100).
5. Among all sites of the "5′UTR" region, those with *p*-value ≤ 0.05 and with average coverage across syngas or fructose bio-replicates > 5 reads were selected.
6. To identify potential TIS candidates within "CDS" or "IG" regions for an operon, we selected all sites with coverages ≥50% of the maximum signal in the "5′UTR" region and with average coverage across syngas or fructose bio-replicates > 20 reads.
7. All sites identified in adjacent sequence positions were collapsed into one site of "size" equal to the number of positions collapsed.

An analogous approach was used to analyze Term-seq read coverage relative to operons, but here we considered for each operon, a genome region comprising the location of the operon and its 3′ flanking (downstream) region up to the downstream operon on the same strand. We characterized each position within this region as hypothetical "3′UTR" region, coding region ("CDS") or intergenic region ("IG") for polycistronic operons and then followed the same procedure as Cappable-seq analysis, considering the "3′UTR" region in place of the "5′UTR" region.

Lastly, we used the following multi-step filtering procedure to determine TISs and T3Es for each operon from the candidate sites identified above (see also Fig. 4).

1. *Site filtering by site coverage and distance from start (for TIS) or stop (for T3E) codon from CDS*. Here, candidate TISs and T3Es were filtered based on their distance from the start (for TIS) or stop (for T3E) codon of the downstream (for TIS) or upstream (for T3E) CDS, $Dist(site, CDS\ start/stop\ codon)$, and based on their coverage in read counts *SiteCov*. We arranged the sites in descending order based on *SiteCov* values and into ascending order based on $Dist(site, CDS\ start/stop\ codon)$ that were then separately partitioned into five quantiles according to their position and signal intensity. As a result, a hypothetical site *i* received the quantile $Q(Dist)_i$ corresponding to its distance relative to the start (stop) codon of the downstream (upstream) coding sequence and the quantile corresponding to $\log_2$ site coverage normalized by the average coverage of all sites from all fructose samples $Q(SiteCov)_i^{fructose}$ or from all syngas samples $Q(SiteCov)_i^{syngas}$. Lastly, the $Q(SiteCov)_i^{growth}$ (growth is either fructose or syngas) and the $Q(Dist)_i$ quantiles of the site *i* were summed up to define the site's composite quantile CQ_i. For each gene (operon), we selected the sites displaying the lowest composite quantile that corresponds to sites which tend to display higher coverage and shorter distances from the respective start or stop codon. If the composite quantile of the site was lower than the central composite quantile, the candidate site passed to the next filtering step. We note that this procedure allows us to retain multiple and different sites per gene (operon) per substrate.
2. *Site filtering by the consistency of 5′UTR read-coverage profile with TIS usage*. Here, candidate 5′UTRs were assessed for consistency with TIS usage as 5′UTRs are expected to display non-uniform read coverage across the TISs. Thus, TISs that contained a stretch of sequence with a length of ≥50% of the total UTR length with a median read coverage ≥5 and ≥50% higher than that for 100 nt upstream of TIS passed to the next filtering steps.

3. *Site filtering by read-coverage profile over the genomic region spanned by gene (operon)*. Here, we assumed read coverage over the gene (operon) to be uniform. Thus, a site passed to the next filtering steps if it is linked to a CDS with a median value of the median read-coverage values computed over 200 nt-long sliding windows being <10% different from the median read-coverage over the full CDS (except if an internal TIS (T3E) is present).
4. *Site clustering by physical proximity*. Here, we selected a representative site if multiple close sites were linked to a gene (operon). Thus, from sites closer than 5 nt from each other, the TIS (T3E) closest to the start (stop) codon of the downstream (upstream) CDS was selected as the primary site. All other sites were considered as alternative sites.

Differential expression analysis of TIS and T3E signals

We quantified differences in TIS and T3E signals (i.e., site coverage) between syngas and fructose using edgeR with the quasi-likelihood F-test procedure[132]. To determine sites with statistically significant differences (q-value < 0.05), we applied the Benjamini–Hochberg procedure to the F-test results, controlling the false discovery rate (FDR) at 5%[133].

Polysome-seq

Sample preparation and sequencing. Before sampling *C. autoethanogenum* chemostat cultures for polysome-seq, translation was arrested by adding chloramphenicol to bioreactors to a final concentration of 0.1 mg/mL. Next, 80 (syngas cultures) or 100 mL (fructose cultures) of culture broth (to match biomass amounts) in four replicate samples were harvested, washed twice, and resuspended in lysis buffer (20 mM Tris HCl pH 8, 140 mM KCl, 40 mM $MgCl_2$, 0.5 mM DTT, 100 µg/mL chloramphenicol, 1 mg/mL heparin, 20 mM EGTA, 1% Triton X-100). After mechanical cell disruption with glass beads, supernatant was flash-frozen in liquid N_2 followed by storage at –80 °C until analysis. Then, mRNA-ribosome complexes were size-separated on a sucrose gradient (10–50% w/v) in a polysome gradient buffer (same composition as lysis buffer except for heparin at a final concentration of 0.5 mg/mL) into 24 subfractions. After protein denaturation and nucleic acid precipitation by adding one volume of 8 M guanidium-HCl and two volumes of absolute ethanol, total RNA was extracted in subfractions using the RNeasy midi kit (Qiagen) combined with on-column DNase I treatment. RNA amount was quantified using a Nanodrop spectrophotometer (Thermo Fisher Scientific). External ERCC RNA spikes (Invitrogen) were added to 1 µg of each total RNA sample according to manufacturer's instructions. The levels of 16S and 23S rRNAs in subfractions were calculated using the Agilent 2100 Bioanalyzer 2100 and used to pool the subfractions into four fractions labeled A to D. Fraction A (from 1 to 4.5 min) consisted of subfractions containing DNA, free RNAs, and free small and large ribosomal subunits. The first peak (Fraction B from 4.5 to 6 min) was attributed to the monosome, Fraction C (from 6 to 8 min) to polysomes with low ribosome density, and Fraction D (from 8 to 12 min) to polysomes with high ribosome density. The average number of ribosomes in Fractions B, C, and D was extrapolated knowing the elution time of the monosome[53] and were found to be similar for syngas and fructose cultures (1.1 ± 0.1 ribosomes in Fraction B, 2.9 ± 0.2 ribosomes in Fraction C, and 7.7 ± 0.5 ribosomes in Fraction D). Total RNA in Fractions A, B, C, and D was ribo-depleted using the RIBO-Zero kit. After fragmentation, the first strand cDNA was synthesized using random hexamer primers. During the second strand cDNA synthesis, dUTPs were replaced with dTTPs in the reaction buffer. The directional library was ready after end repair, A-tailing, adapter ligation, size selection, USER enzyme digestion, amplification, and purification. Finally, libraries were sequenced using the Illumina Novaseq X Plus Series platform with 2 × 150 bp cycles (paired-end).

Quantification of transcript abundances. Firstly, reads with >10% of undetermined bases (N) and reads with >50% of bases with Qscore ≤ 5 were excluded. Secondly, the ERCC RNA spikes were used to determine the linearity range between read counts and RNA concentration and thus features among the 4,043 LAbrini genes and 92 ERCC RNAs with <10 read counts were excluded for reliable quantification (259 and 264 features for fructose and syngas, respectively). Reads trimmed of Illumina adapters were then mapped to the genome of *C. autoethanogenum* strain LAbrini (GenBank CP110420.1) and ERCC RNA spikes using Bowtie2[134] and read counting was performed using the featureCounts function within Rsubread[135]. To account for variations in sample preparation and analysis from ribodepletion to sequencing, two normalization steps were used. Firstly, we applied the RUV method to remove unwanted variation[136] using the ERCC RNA spikes introduced in each fraction before the ribodepletion step: we obtained $N_{i,j,k\ NormRUVg}$, with the count of the transcript i, in the fraction j, and bio-replicate k after normalizing with the RUV method, with $i \in \{1,\ldots,3876\}$, $j \in \{A,B,C,D\}$ and $k \in \{1,2,3\}$ on fructose and with $i \in \{1,\ldots,3871\}$, $j \in \{A,B,C,D\}$ and $k \in \{1,2,3\}$ on syngas. Secondly, we accounted for the variability in the initial amount of total RNA between fractions as a constant 0.5 µg of total RNA was taken in each fraction for ribodepletion: we obtained the final normalized count of the transcript i, in the fraction j, and bio-replicate k as $N_{i,j,k} = N_{i,j,k\ NormRUVg}\ x\ total\ RNA\ quantity_{j,k}/0.5$. Finally, for each transcript i, we calculated the proportion of RNA copies in each fraction j for each bio-replicate k:

$$\text{RNA proportion in fraction}_{i,j,k}(\%) = N_{i,j,k} \times 100 / \sum_{j=A}^{D} N_{i,j,k} \qquad (1)$$

Consistency analysis of bio-replicates. Due to the lower-than-expected correlation between fractional mRNA counts of some bio-replicates (Supplementary Fig. 3), we assessed data consistency between bio-replicates within both chemostat datasets by three complementary methods suited for compositional data, such as polysome-seq: correlation analysis, compositional distance analysis, and principal component analysis (PCA). Firstly, we computed the Spearman's rank correlation coefficient (ρ) of mRNA counts per polysomal gradient fraction from total counts between bio-replicates. A bio-replicate was determined an outlier if it showed the highest number of poorly correlated polysomal fractions; a fraction was considered poorly correlated if its data correlated poorly ($\rho < 0.7$) with the other bio-replicates which in turn correlated between each other with $\rho > 0.7$. Secondly, we calculated the average of all mRNA counts for each fraction and bio-replicate, then centered-ln-ratio transformed the averages, and lastly computed the Aitchison's distance between each pair of bio-replicates. A bio-replicate was determined an outlier if it showed the maximal average Aitchison's distance[137] from the other bio-replicates that was greater than the median distance observed across syngas and fructose. Thirdly, we collated all mRNA counts for each fraction and bio-replicate as a concatenated dataset, then centered-ln-ratio transformed gene compositional data, and lastly performed PCA to compute the average distances between the centroids of each pair of bio-replicates. A bio-replicate was determined an outlier if its centroid showed the maximal average distance from the centroids of the other bio-replicates that was greater than the median distance observed across syngas and fructose. Finally, we assembled the information from the three approaches and determined the bio-replicate an outlier that was found to be an outlier according to the highest number of approaches.

Determination of DTLs. We used three complementary metrics to quantify translational regulation and finally determined DTLs using a consensus approach (CONSENSUS) over the three metrics.

First, for the TL-STATUS metric, we firstly calculated for each gene its translation status in both syngas and fructose as the ratio between

the sum of the mRNA proportions quantified in the ribosome-bound and ribosome-free fractions. Secondly, subtracting the fructose value from syngas, we quantified the absolute difference of the translation status per gene between syngas and fructose (TL-STATUS). Genes were then ranked by decreasing order of the calculated TL-STATUS values for evaluation with the CONSENSUS approach (see below).

Second, as the TL-PROFILE metric, we calculated for each gene the difference in its polysome profiles between syngas and fructose as the variance-weighted Aitchison's distance of the centered-ln-ratio transformed compositional data by weighing the difference between the individual fractions by pooled variance across syngas and fructose bioreplicates. Genes were then ranked by decreasing order of the calculated TL-PROFILE values for evaluation with the CONSENSUS approach.

Third, as the POLY-FRACTIONS metric, we estimated 95% confidence intervals (CI) for each polysome fraction and gene by bootstrapping from a resampling distribution and then identified fractions with differential mRNA proportions if their computed CI did not cross the null value. This metric quantified both the number of statistically different fractions per gene and the maximal difference across fractions between conditions. Genes were then ranked by decreasing order of both features for evaluation with the CONSENSUS approach.

Lastly, to account for the different nature of translational regulation captured by each metric, we used a CONSENSUS approach that ranked genes based on the average of the ranks obtained across the three metrics. We determined DTLs as genes within the top 5% of the CONSENSUS ranking.

RNA-seq

Sample preparation and sequencing. The same cell pellets as for polysome-seq were used for RNA-seq (see above for sampling details). Total RNA from frozen samples was extracted using the RNeasy Midi Kit combined with on-column DNase I treatment. RNA amount was quantified using the Nanodrop spectrophotometer and RNA integrity validated using the Agilent Bioanalyzer 2100. External ERCC RNA spikes were added to 1 μg of each total RNA sample according to manufacturer's instructions. Total RNA was ribo-depleted using the RIBO-Zero kit and size distribution evaluated with the Agilent Bioanalyzer 2100. After fragmentation, the first strand cDNA was synthesized using random hexamer primers. During the second strand cDNA synthesis, dUTPs were replaced with dTTPs in the reaction buffer. The directional library was ready after end repair, A-tailing, adapter ligation, size selection, USER enzyme digestion, amplification, and purification. Finally, libraries were sequenced using the Illumina Novaseq X Plus Series platform with 2× 150 bp cycles (paired-end).

Quantification of transcript abundances and differential expression analysis. The ERCC RNA spikes were used to determine the linearity range between read counts and RNA concentration and thus transcripts with <10 read counts were excluded for reliable quantification. Additionally, reads with >10% of undetermined bases (N) and reads with >50% of bases with Qscore ≤ 5 were excluded. Reads trimmed of Illumina adapters were then mapped to the genome of *C. autoethanogenum* strain LAbrini (GenBank CP110420.1) and ERCC RNA spikes using Bowtie2[134] and read counting was performed using the featureCounts function within Rsubread[135]. Raw library sizes were normalized across the samples using the normLibSizes function within edgeR[138]. Differential expression analysis between syngas and fructose cultures was performed within edgeR using the quasi-likelihood F-test as per the glmQLFTest function[139]. To determine genes with statistically different expression (q-value < 0.05), we applied the Benjamini–Hochberg procedure to the F-test results controlling the false discovery rate (FDR) at 5%[133].

Identification of RNA-binding proteins

Potential RNA-binding proteins in *C. autoethanogenum* were predicted using PRONTO-TK[45], a neural network-based framework for protein function prediction. The ProtT5-XL model converts protein sequences into 1024-dimensional vector embeddings that capture learned biochemical properties (hydrophobicity, charge, size) and structural propensities (secondary structure preferences, fold patterns) derived from evolutionary relationships in the model's training data. Proteins predicted with posterior probabilities above the confidence threshold of 0.75 were retained as candidate RBPs for downstream analyses of RBP–RNA interactions.

Prediction of protein-RNA interactions

We employed catRAPID omics v2[46] to predict protein–RNA interactions between the candidate RBPs and differentially regulated genes (DTRs and DTLs) at genome scale. The tool accepts custom input protein and RNA sequences and computes interaction scores based on updated precompiled libraries. The multi-parametric rating system of catRAPID predictions integrates multiple scores[140]—interaction propensity, RBP propensity, and presence of known RNA-binding motifs—to provide final scores ranging between 0 and 1. Protein-RNA interactions predicted by catRAPID were retained if the corresponding Z-scores pertaining to the interaction propensity and the final scores were ranked in the top 25% positions.

Reporting summary

Further information on research design is available in the Nature Portfolio Reporting Summary linked to this article.

Data availability

Additional data can be found in Supplementary Data. All raw sequencing data generated in this study have been deposited at the European Nucleotide Archive under project accession code PRJEB102336. Source data are provided with this paper.

Code availability

Code[141,142] has been deposited at Zenodo under https://doi.org/10.5281/zenodo.20374071 (Version 2.0) [https://doi.org/10.5281/zenodo.13272725] and under https://doi.org/10.5281/zenodo.20374300 (Version 1.5) [https://doi.org/10.5281/zenodo.20374299].

References

1. Fackler, N. et al. Stepping on the gas to a circular economy: accelerating development of carbon-negative chemical production from gas fermentation. *Annu. Rev. Chem. Biomol. Eng.* **12**, 439–470 (2021).
2. Köpke, M. & Simpson, S. D. Pollution to products: recycling of 'above ground' carbon by gas fermentation. *Curr. Opin. Biotechnol.* **65**, 180–189 (2020).
3. Pavan, M. et al. Advances in systems metabolic engineering of autotrophic carbon oxide-fixing biocatalysts towards a circular economy. *Metab. Eng.* **71**, 117–141 (2022).
4. Poehlein, A. et al. Advanced aspects of acetogens. *Bioresour. Technol.* **427**, 131913 (2025).
5. Wood, H. G. Life with CO or CO_2 and H_2 as a source of carbon and energy. *Faseb J.* **5**, 156–163 (1991).
6. Drake, H. L., Küsel, K., Matthies, C. Acetogenic prokaryotes. in: *The Prokaryotes* (eds. Dworkin, M. et al.) 354–420 (Springer, 2006).
7. Cotton, C. A., Edlich-Muth, C. & Bar-Even, A. Reinforcing carbon fixation: CO_2 reduction replacing and supporting carboxylation. *Curr. Opin. Biotech.* **49**, 49–56 (2018).
8. Ragsdale, S. W. & Pierce, E. Acetogenesis and the Wood-Ljungdahl pathway of CO(2) fixation. *Biochim. Biophys. Acta* **1784**, 1873–1898 (2008).

9. Heffernan, J. K., Mahamkali, V., Valgepea, K., Marcellin, E. & Nielsen, L. K. Analytical tools for unravelling the metabolism of gas-fermenting Clostridia. *Curr. Opin. Biotechnol.* **75**, 102700 (2022).
10. Bae, J., Park, C., Jung, H., Jin, S. & Cho, B. K. Harnessing acetogenic bacteria for one-carbon valorization toward sustainable chemical production. *RSC Chem. Biol.* **5**, 812–832 (2024).
11. Jin, S. et al. Synthetic biology on acetogenic bacteria for highly efficient conversion of C1 gases to biochemicals. *Int. J. Mol. Sci.* **21**, 7639 (2020).
12. Greene, J., Daniell, J., Köpke, M., Broadbelt, L. & Tyo, K. E. J. Kinetic ensemble model of gas fermenting *Clostridium autoethanogenum* for improved ethanol production. *Biochem. Eng. J.* **148**, 46–56 (2019).
13. Valgepea, K. et al. Absolute proteome quantification in the gas-fermenting acetogen *Clostridium autoethanogenum*. *mSystems* **7**, e0002622 (2022).
14. Mahamkali, V. et al. Redox controls metabolic robustness in the gas-fermenting acetogen *Clostridium autoethanogenum*. *Proc. Natl. Acad. Sci. USA*. **117**, 13168–13175 (2020).
15. Song, Y. et al. Genome-scale analysis of syngas fermenting acetogenic bacteria reveals the translational regulation for its autotrophic growth. *BMC Genom.* **19**, 837 (2018).
16. Song, Y. et al. Transcriptome and translatome of CO_2 fixing acetogens under heterotrophic and autotrophic conditions. *Sci. Data* **8**, 51 (2021).
17. Al-Bassam et al. Optimization of carbon and energy utilization through differential translational efficiency. *Nat. Commun.* **9**, 4474 (2018).
18. Shin, J. et al. Genome-scale analysis of *Acetobacterium woodii* identifies translational regulation of acetogenesis. *mSystems* **6**, e0069621 (2021).
19. Re, A. Translational efficiency in gas-fermenting bacteria: adding a new layer of regulation to gene expression in acetogens. *iScience* **26**, 108383 (2023).
20. Ng Kwan Lim, E., Sasseville, C., Carrier, M. C. & Massé, E. Keeping up with RNA-based regulation in bacteria: new roles for RNA binding proteins. *Trends Genet.* **37**, 86–97 (2021).
21. Roberts, J. W. Termination factor for RNA synthesis. *Nature* **224**, 1168–1174 (1969). (1969).
22. Figueroa-Bossi, N. et al. RNA remodeling by bacterial global regulator CsrA promotes Rho-dependent transcription termination. *Genes Dev.* **28**, 1239–1251 (2014).
23. Holmqvist, E. & Vogel, J. RNA-binding proteins in bacteria. *Nat. Rev. Microbiol.* **16**, 601–615 (2018).
24. Mondal, S., Yakhnin, A. V., Sebastian, A., Albert, I. & Babitzke, P. NusA-dependent transcription termination prevents misregulation of global gene expression. *Nat. Microbiol.* **1**, 15007 (2016).
25. Kumarevel, T., Mizuno, H. & Kumar, P. K. Structural basis of HutP-mediated anti-termination and roles of the Mg2+ ion and L-histidine ligand. *Nature* **434**, 183–191 (2005).
26. Bechhofer, D. H. & Deutscher, M. P. Bacterial ribonucleases and their roles in RNA metabolism. *Crit. Rev. Biochem. Mol. Biol.* **54**, 242–300 (2019).
27. Ellis, M. J., Trussler, R. S. & Haniford, D. B. Hfq binds directly to the ribosome-binding site of IS10 transposase mRNA to inhibit translation. *Mol. Microbiol.* **96**, 633–650 (2015).
28. Rüttiger, A. S. et al. The global RNA-binding protein RbpB is a regulator of polysaccharide utilization in *Bacteroides thetaiotaomicron*. *Nat.Commun.* **16**, 208 (2025).
29. Ignatov, D. et al. RNA-binding protein YebC enhances translation of proline-rich amino acid stretches in bacteria. *Nat. Commun.* **16**, 6262 (2025).
30. McQuail, J. et al. Condensation of the RNA chaperone Hfq is coupled to inhibition of glucose uptake and contributes to the stabilization of regulatory RNAs in nitrogen-starved *Escherichia coli*. *Nucleic Acids Res.* **53**, gkaf1006 (2025).
31. Papenfort, K. & Melamed, S. Small RNAs, large networks: post-transcriptional regulons in gram-negative bacteria. *Annu. Rev. Microbiol.* **77**, 23–43 (2023).
32. Fuchs, M. et al. An RNA-centric global view of *Clostridioides difficile* reveals broad activity of Hfq in a clinically important gram-positive bacterium. *Proc. Natl. Acad. Sci. USA*. **118**, e2103579118 (2021).
33. Piatek, P. et al. Agr Quorum Sensing influences the Wood-Ljungdahl pathway in *Clostridium autoethanogenum*. *Sci. Rep.* **12**, 411 (2022).
34. de Lima, L. A. et al. Faster Growth Enhances Low Carbon Fuel and Chemical Production Through Gas Fermentation. *Front. Bioeng. Biotechnol.* **10**, 879578 (2022).
35. Nwaokorie, U. J. et al. Deletion of genes linked to the C1-fixing gene cluster affects growth, by-products, and proteome of *Clostridium autoethanogenum*. *Front. Bioeng. Biotechnol.* **11**, 1167892 (2023).
36. Ingelman, H. et al. Autotrophic adaptive laboratory evolution of the acetogen *Clostridium autoethanogenum* delivers the gas-fermenting strain LAbrini with superior growth, products, and robustness. *New Biotech.* **83**, 1–15 (2024).
37. Heffernan, J. et al. Adaptive laboratory evolution of *Clostridium autoethanogenum* to metabolize CO_2 and H_2 enhances growth rates in chemostat and unravels proteome and metabolome alterations. *Microb. Biotechnol.* **17**, e14452 (2024).
38. Davin, M. E. et al. *Clostridium autoethanogenum* alters cofactor synthesis, redox metabolism, and lysine-acetylation in response to elevated H_2:CO feedstock ratios for enhancing carbon capture efficiency. *Biotechnol. Biofuels Bioprod.* **17**, 119 (2024).
39. Liew, F. E. et al. Carbon-negative production of acetone and isopropanol by gas fermentation at industrial pilot scale. *Nat. Biotechnol.* **40**, 335–344 (2022).
40. Dykstra, J. C. et al. Metabolic engineering of *Clostridium autoethanogenum* for ethyl acetate production from CO. *Microb. Cell. Fact.* **21**, 243 (2022).
41. Castello, A. et al. System-wide identification of RNA-binding proteins by interactome capture. *Nat. Protoc.* **8**, 491–500 (2013).
42. Stenum, T. S. et al. RNA interactome capture in *Escherichia coli* globally identifies RNA-binding proteins. *Nucleic Acids Res.* **51**, 4572–4587 (2023).
43. Liu, Y. J., Wang, X., Sun, Y. & Feng, Y. Bacterial 5′ UTR: A treasure-trove for post-transcriptional regulation. *Biotechnol. Adv.* **78**, 108478 (2025).
44. Menendez-Gil, P. & Toledo-Arana, A. Bacterial 3′UTRs: A Useful Resource in Post-transcriptional Regulation. *Front. Mol. Biosci.* **7**, 617633 (2021).
45. Politano, G., Benso, A., Rehman, H. U. & Re, A. PRONTO-TK: a user-friendly PROtein Neural neTwOrk tool-kit for accessible protein function prediction. *NAR Genom. Bioinform.* **6**, lqae112 (2024).
46. Armaos, A., Colantoni, A., Proietti, G., Rupert, J. & Tartaglia, G. G. catRAPID omics v2.0: going deeper and wider in the prediction of protein-RNA interactions. *Nucleic Acids Res.* **49**, W72–W79 (2021).
47. Adamberg, K., Valgepea, K. & Vilu, R. Advanced continuous cultivation methods for systems microbiology. *Microbiology* **161**, 1707–1719 (2015).
48. Hoskisson, P. A. & Hobbs, G. Continuous culture–making a comeback? *Microbiology* **151**, 3153–3159 (2005).
49. Weiss, M. C. et al. The physiology and habitat of the last universal common ancestor. *Nat. Microbiol.* **1**, 16116 (2016).
50. Marcellin, E. et al. Low carbon fuels and commodity chemicals from waste gases – systematic approach to understand energy metabolism in a model acetogen. *Green Chem.* **18**, 3020–3028 (2016).

51. Arava, Y. et al. Genome-wide analysis of mRNA translation profiles in *Saccharomyces cerevisiae*. *Proc. Natl. Acad. Sci. USA*. **100**, 3889–3894 (2003).
52. Nguyen, H. L. et al. Synergistic regulation of transcription and translation in *Escherichia coli* revealed by codirectional increases in mRNA concentration and translation efficiency. *Microbiol. Spectr.* **10**, e0204121 (2022).
53. Picard, F. et al. Bacterial translational regulations: high diversity between all mRNAs and major role in gene expression. *BMC Genom.* **13**, 528 (2012).
54. Lackner, D. H. et al. A network of multiple regulatory layers shapes gene expression in fission yeast. *Mol. Cell* **26**, 145–155 (2007).
55. Kanehisa, M., Sato, Y. & Morishima, K. BlastKOALA and GhostKOALA: KEGG tools for functional characterization of genome and metagenome sequences. *J. Mol. Biol.* **428**, 726–731 (2016).
56. Mistry, J. et al. Pfam: The protein families database in 2021. *Nucleic Acids Res.* **49**, D412–D419 (2021).
57. Aseev, L. V., Koledinskaya, L. S. & Boni, I. V. Extraribosomal functions of bacterial ribosomal proteins-an update, 2023. *Int. J. Mol. Sci.* **25**, 2957 (2024).
58. Hess, V. et al. Occurrence of ferredoxin:NAD(+) oxidoreductase activity and its ion specificity in several Gram-positive and Gram-negative bacteria. *PeerJ* **4**, e1515 (2016).
59. Tremblay, P. L., Zhang, T., Dar, S. A., Leang, C. & Lovley, D. R. The Rnf complex of *Clostridium ljungdahlii* is a proton-translocating ferredoxin:NAD+ oxidoreductase essential for autotrophic growth. *mBio* **4**, e00406–e00412 (2012).
60. Meyer, M. M. rRNA mimicry in RNA regulation of gene expression. *Microbiol. Spectr.* **6**, https://doi.org/10.1128/microbiolspec.rwr-0006-2017 (2018).
61. Kashiwagi, K. & Igarashi, K. Nonspecific inhibition of *Escherichia coli* ornithine decarboxylase by various ribosomal proteins: detection of a new ribosomal protein possessing strong antizyme activity. *Biochim. Biophys. Acta.* **911**, 180–190 (1987).
62. Tan, Q., Gou, L., Fan, T. P. & Cai, Y. Enzymatic properties of ornithine decarboxylase from *Clostridium aceticum* DSM1496. *Biotechnol. Appl. Biochem.* **71**, 525–535 (2024).
63. Daume, M., Uhl, M., Backofen, R. & Randau, L. RIP-Seq suggests translational regulation by L7Ae in archaea. *mBio* **8**, e00730-17 (2017).
64. Berges, M. et al. Iron Regulation in *Clostridioides difficile*. *Front. Microbiol.* **9**, 3183 (2018).
65. Cernat, R. C. & Scott, K. P. Evaluation of novel assays to assess the influence of different iron sources on the growth of *Clostridium difficile*. *Anaerobe* **18**, 298–304 (2012).
66. Ettwiller, L., Buswell, J., Yigit, E. & Schildkraut, I. A novel enrichment strategy reveals unprecedented number of novel transcription start sites at single base resolution in a model prokaryote and the gut microbiome. *BMC Genom.* **17**, 199 (2016).
67. Boutard, M. et al. Global repositioning of transcription start sites in a plant-fermenting bacterium. *Nat. Commun.* **7**, 13783 (2016).
68. Sharma, C. M. et al. The primary transcriptome of the major human pathogen *Helicobacter pylori*. *Nature* **464**, 250–255 (2010).
69. Dar, D. et al. Term-seq reveals abundant ribo-regulation of antibiotics resistance in bacteria. *Science* **352**, aad9822 (2016).
70. Mejía-Almonte, C. et al. Redefining fundamental concepts of transcription initiation in bacteria. *Nat. Rev. Genet.* **21**, 699–714 (2020).
71. de Souza Pinto Lemgruber, R. et al. A TetR-family protein (CAETHG_0459) activates transcription from a new promoter motif associated with essential genes for autotrophic growth in acetogens. *Front. Microbiol.* **10**, 2549 (2019).
72. Bailey, T. L. et al. MEME SUITE: tools for motif discovery and searching. *Nucleic Acids Res.* **37**, W202–W208 (2009).
73. Mandal, P. K., Collie, G. W., Srivastava, S. C., Kauffmann, B. & Huc, I. Structure elucidation of the Pribnow box consensus promoter sequence by racemic DNA crystallography. *Nucleic Acids Res.* **44**, 5936–5943 (2016).
74. Graves, M. C. & Rabinowitz, J. C. In vivo and in vitro transcription of the *Clostridium pasteurianum* ferredoxin gene. Evidence for "extended" promoter elements in gram-positive organisms. *J. Biol. Chem.* **261**, 11409–11415 (1986).
75. Helmann, J. D. Compilation and analysis of *Bacillus subtilis* sigma A-dependent promoter sequences: evidence for extended contact between RNA polymerase and upstream promoter DNA. *Nucleic Acids Res.* **23**, 2351–2360 (1995).
76. Ross, W. et al. A third recognition element in bacterial promoters: DNA binding by the alpha subunit of RNA polymerase. *Science* **262**, 1407–1413 (1993).
77. Turnbough, C. L. Jr Regulation of bacterial gene expression by transcription attenuation. *Microbiol. Mol. Biol. Rev.* **83**, e00019-19 (2019).
78. Song, Y. et al. Development of highly characterized genetic bioparts for efficient gene expression in CO_2-fixing *Eubacterium limosum*. *Metab. Eng.* **72**, 215–226 (2022).
79. Bae, J. et al. Multi-omics analysis reveals the genetic basis for rapid CO_2 utilization in the acetogenic bacterium *Sporomusa sphaeroides* KIAC. *mSystems* **10**, e0045125 (2025).
80. Robinson, J. T. et al. Integrative genomics viewer. *Nat. Biotechnol.* **29**, 24–26 (2011).
81. Ingelman, H., Shaikh, K. M. & Valgepea, K. Reverse-engineered gas-fermenting acetogen strains recover enhanced phenotypes from autotrophic adaptive laboratory evolution. *Microb. Biotechnol.* **18**, e70208 (2025).
82. Galperin, M. Y. Structural classification of bacterial response regulators: diversity of output domains and domain combinations. *J. Bacteriol.* **188**, 4169–4182 (2006).
83. West, A. H. & Stock, A. M. Histidine kinases and response regulator proteins in two-component signaling systems. *Trends Biochem. Sci.* **26**, 369–376 (2001).
84. Ho, Y. S., Burden, L. M. & Hurley, J. H. Structure of the GAF domain, a ubiquitous signaling motif and a new class of cyclic GMP receptor. *EMBO J.* **19**, 5288–5299 (2001).
85. Xing, J., Gumerov, V. M. & Zhulin, I. B. Origin and functional diversification of PAS domain, a ubiquitous intracellular sensor. *Sci. Adv.* **9**, eadi4517 (2023).
86. Matilla, M. A., Velando, F., Martín-Mora, D., Monteagudo-Cascales, E. & Krell, T. A catalogue of signal molecules that interact with sensor kinases, chemoreceptors and transcriptional regulators. *Fems Microbiol. Rev.* **46**, fuab043 (2022).
87. Shingler, V. Signal sensing by sigma 54-dependent regulators: derepression as a control mechanism. *Mol. Microbiol.* **19**, 409–416 (1996).
88. Francke, C. et al. Comparative analyses imply that the enigmatic Sigma factor 54 is a central controller of the bacterial exterior. *BMC Genom.* **12**, 385 (2011).
89. Szurmant, H., Bu, L., Brooks, C. L. 3rd & Hoch, J. A. An essential sensor histidine kinase controlled by transmembrane helix interactions with its auxiliary proteins. *Proc. Natl. Acad. Sci. USA.* **105**, 5891–5896 (2008).
90. Fukushima, T. et al. A role for the essential YycG sensor histidine kinase in sensing cell division. *Mol. Microbiol.* **79**, 503–522 (2011).
91. Woods, C. et al. Required gene set for autotrophic growth of *Clostridium autoethanogenum*. *Appl. Environ. Microbiol.* **88**, e0247921 (2022).
92. Westphal, L., Wiechmann, A., Baker, J., Minton, N. P. & Müller, V. The Rnf complex is an energy-coupled transhydrogenase essential to reversibly link cellular NADH and ferredoxin pools in the

acetogen *Acetobacterium woodii*. *J. Bacteriol.* **200**, e00357–18 (2018).
93. UniProt Consortium UniProt: the Universal Protein Knowledgebase in 2025. *Nucleic Acids Res.* **53**, D609–D617 (2025).
94. Briani, F., Carzaniga, T. & Dehò, G. Regulation and functions of bacterial PNPase. *Wiley Interdiscip. Rev. RNA* **7**, 241–258 (2016).
95. Dendooven, T. et al. A cooperative PNPase-Hfq-RNA carrier complex facilitates bacterial riboregulation. *Mol. Cell* **81**, 2901–2913.e5 (2021).
96. Schubert, H. L., Blumenthal, R. M. & Cheng, X. Many paths to methyltransfer: a chronicle of convergence. *Trends Biochem. Sci.* **28**, 329–335 (2003).
97. Shahbabian, K., Jamalli, A., Zig, L., Putzer, H. & RNase, Y. A novel endoribonuclease, initiates riboswitch turnover in *Bacillus subtilis*. *Embo J.* **28**, 3523–3533 (2009).
98. DiChiara, J. M., Liu, B., Figaro, S., Condon, C. & Bechhofer, D. H. Mapping of internal monophosphate 5′ ends of *Bacillus subtilis* messenger RNAs and ribosomal RNAs in wild-type and ribonuclease-mutant strains. *Nucleic Acids Res.* **44**, 3373–3389 (2016).
99. Durand, S., Gilet, L., Bessières, P., Nicolas, P. & Condon, C. Three essential ribonucleases-RNase Y, J1, and III-control the abundance of a majority of *Bacillus subtilis* mRNAs. *PLoS Genet.* **8**, e1002520 (2012).
100. Głów, D. et al. Sequence-specific cleavage of dsRNA by mini-III RNase. *Nucleic Acids Res.* **43**, 2864–2873 (2015).
101. Mandell, Z. F. et al. Comprehensive transcription terminator atlas for *Bacillus subtilis*. *Nat. Microbiol.* **7**, 1918–1931 (2022).
102. Vogel, U. & Jensen, K. F. NusA is required for ribosomal antitermination and for modulation of the transcription elongation rate of both antiterminated RNA and mRNA. *J. Biol. Chem.* **272**, 12265–12271 (1997).
103. Parthun, M., Long, M. E. & Hemann, E. A. Established and emerging roles of DEAD/H-Box helicases in regulating infection and immunity. *Immunol. Rev.* **329**, e13426 (2025).
104. Schaening-Burgos, C., LeBlanc, H., Fagre, C., Li, G. W. & Gilbert, W. V. RluA is the major mRNA pseudouridine synthase in *Escherichia coli*. *PLoS Genet.* **20**, e1011100 (2024).
105. Valgepea, K. et al. Maintenance of ATP homeostasis triggers metabolic shifts in gas-fermenting acetogens. *Cell Syst.* **4**, 505–515.e5 (2017).
106. de Crécy-Lagard, V. & Jaroch, M. Functions of bacterial tRNA modifications: from ubiquity to diversity. *Trends Microbiol.* **29**, 41–53 (2021).
107. Valgepea, K. et al. H_2 drives metabolic rearrangements in gas-fermenting *Clostridium autoethanogenum*. *Biotechnol. Biofuels* **11**, 55 (2018).
108. Cox, R. A. Quantitative relationships for specific growth rates and macromolecular compositions of *Mycobacterium tuberculosis*, *Streptomyces coelicolor* A3(2) and *Escherichia coli* B/r: an integrative theoretical approach. *Microbiology* **150**, 1413–1426 (2004).
109. Stouthamer, A. H. A theoretical study on the amount of ATP required for synthesis of microbial cell material. *Antonie van Leeuwenhoek* **39**, 545–565 (1973).
110. Johnson, G. E., Lalanne, J. B., Peters, M. L. & Li, G. W. Functionally uncoupled transcription-translation in *Bacillus subtilis*. *Nature* **585**, 124–128 (2020).
111. Babitzke, P. & Yanofsky, C. Reconstitution of *Bacillus subtilis* trp attenuation in vitro with TRAP, the trp RNA-binding attenuation protein. *Proc. Natl. Acad. Sci. USA.* **90**, 133–137 (1993).
112. Oda, M., Kobayashi, N., Ito, A., Kurusu, Y. & Taira, K. cis-acting regulatory sequences for antitermination in the transcript of the *Bacillus subtilis* hut operon and histidine-dependent binding of HutP to the transcript containing the regulatory sequences. *Mol. Microbiol.* **35**, 1244–1254 (2000).
113. Aymerich, S. & Steinmetz, M. Specificity determinants and structural features in the RNA target of the bacterial antiterminator proteins of the BglG/SacY family. *Proc. Natl. Acad. Sci. USA.* **89**, 10410–10414 (1992).
114. Turner, R. J., Lu, Y. & Switzer, R. L. Regulation of the *Bacillus subtilis* pyrimidine biosynthetic (pyr) gene cluster by an autogenous transcriptional attenuation mechanism. *J. Bacteriol.* **176**, 3708–3722 (1994).
115. Julia Dierksheide, K., Battaglia, R. A. & Li, G. W. How do bacteria tune transcription termination efficiency? *Curr. Opin. Microbiol.* **82**, 102557 (2024).
116. Merino, E. & Yanofsky, C. Transcription attenuation: a highly conserved regulatory strategy used by bacteria. *Trends Genet.* **21**, 260–264 (2005).
117. Peters, J. M., Vangeloff, A. D. & Landick, R. Bacterial transcription terminators: the RNA 3′-end chronicles. *J. Mol. Biol.* **412**, 793–813 (2011).
118. Millman, A., Dar, D., Shamir, M. & Sorek, R. Computational prediction of regulatory, premature transcription termination in bacteria. *Nucleic Acids Res.* **45**, 886–893 (2017).
119. Metelev, M. & Johansson, M. A complex between IF2 and NusA suggests early coupling of transcription-translation. *Nat. Commun.* **16**, 6906 (2025).
120. Spanka, D. T., Reuscher, C. M. & Klug, G. Impact of PNPase on the transcriptome of *Rhodobacter sphaeroides* and its cooperation with RNase III and RNase E. *BMC Genom.* **22**, 106 (2021).
121. Braun, F., Durand, S. & Condon, C. Initiating ribosomes and a 5′/3′-UTR interaction control ribonuclease action to tightly couple *B. subtilis* hbs mRNA stability with translation. *Nucleic Acids Res.* **45**, 11386–11400 (2017).
122. Khemici, V., Prados, J., Linder, P. & Redder, P. Decay-initiating endoribonucleolytic cleavage by RNase Y is kept under tight control via sequence preference and sub-cellular localisation. *PLoS Genet.* **11**, e1005577 (2015).
123. Taggart, J. C. et al. A high-resolution view of RNA endonuclease cleavage in *Bacillus subtilis*. *Nucleic Acids Res.* **53**, gkaf030 (2025).
124. Condon, C., Rourera, J., Brechemier-Baey, D. & Putzer, H. Ribonuclease M5 has few, if any, mRNA substrates in *Bacillus subtilis*. *J. Bacteriol.* **184**, 2845–2849 (2002).
125. DiMari, J. F. & Bechhofer, D. H. Initiation of mRNA decay in *Bacillus subtilis*. *Mol. Microbiol.* **7**, 705–717 (1993).
126. Lioliou, E. et al. Global regulatory functions of the *Staphylococcus aureus* endoribonuclease III in gene expression. *PLoS Genet.* **8**, e1002782 (2012).
127. Dai, Q. et al. Quantitative sequencing using BID-seq uncovers abundant pseudouridines in mammalian mRNA at base resolution. *Nat. Biotechnol.* **41**, 344–354 (2023).
128. Eyler, D. E. et al. Pseudouridinylation of mRNA coding sequences alters translation. *Proc. Natl. Acad. Sci. USA.* **116**, 23068–23074 (2019).
129. Svitkin, Y. V. et al. N1-methyl-pseudouridine in mRNA enhances translation through eIF2α-dependent and independent mechanisms by increasing ribosome density. *Nucleic Acids Res.* **45**, 6023–6036 (2017).
130. Gilbert, W. V. Recent developments, opportunities, and challenges in the study of mRNA pseudouridylation. *RNA* **30**, 530–536 (2024).
131. Dobin, A. et al. STAR: ultrafast universal RNA-seq aligner. *Bioinformatics* **29**, 15–21 (2013).
132. Lun, A. T., Chen, Y. & Smyth, G. K. It's DE-licious: a recipe for differential expression analyses of RNA-seq experiments using quasi-likelihood methods in edgeR. *Methods Mol. Biol.* **1418**, 391–416 (2016).

133. Benjamini, Y. & Hochberg, Y. Controlling the false discovery rate: a practical and powerful approach to multiple testing. *J. R. Stat. Soc. Ser. B Stat. Methodol.* **57**, 289–300 (1995).
134. Langmead, B. & Salzberg, S. L. Fast gapped-read alignment with Bowtie 2. *Nat. Methods* **9**, 357–359 (2012).
135. Liao, Y., Smyth, G. K. & Shi, W. The Subread aligner: fast, accurate and scalable read mapping by seed-and-vote. *Nucleic Acids Res.* **41**, e108 (2013).
136. Risso, D., Ngai, J., Speed, T. P. & Dudoit, S. Normalization of RNA-seq data using factor analysis of control genes or samples. *Nat. Biotechnol.* **32**, 896–902 (2014).
137. Aitchison, J. *The Statistical Analysis of Compositional Data* (Chapman and Hall, 1986).
138. Chen, Y., Chen, L., Lun, A. T. L., Baldoni, P. L. & Smyth, G. K. edgeR v4: powerful differential analysis of sequencing data with expanded functionality and improved support for small counts and larger datasets. *Nucleic Acids Res.* **53**, gkaf018 (2025).
139. Lund, S. P., Nettleton, D., McCarthy, D. J., & Smyth, G. K. Detecting differential expression in RNA-sequence data using quasi-likelihood with shrunken dispersion estimates. *Stat. Appl. Genet. Mol. Biol*. 11, /j/sagmb.2012.11.issue-5/1544-6115.1826/1544-6115.1826.xml (2012).
140. Bellucci, M., Agostini, F., Masin, M. & Tartaglia, G. G. Predicting protein associations with long noncoding RNAs. *Nat Methods* **8**, 444–445 (2011).
141. Re, A. et al. Systems-level analysis predicts no autotrophy-linked protein-RNA interactions in *Clostridium autoethanogenum*, Zenodo, https://doi.org/10.5281/zenodo.20374071 (2026).
142. Re, A. et al. Systems-level analysis predicts no autotrophy-linked protein-RNA interactions in *Clostridium autoethanogenum*, Zenodo, https://doi.org/10.5281/zenodo.20374300 (2026).
143. Cantalapiedra, C. P., Hernández-Plaza, A., Letunic, I., Bork, P. & Huerta-Cepas, J. eggNOG-mapper v2: functional annotation, orthology assignments, and domain prediction at the metagenomic scale. *Mol. Biol. Evol.* **38**, 5825–5829 (2021).

Acknowledgements

Figure 1 source attributions: bubbles icon designed by kerismaker; sugar-cube icon designed by Freepik; bioreactor icons designed by Dewi Sari; machine icon designed by Freepik; machine-learning icon designed by gravisio; planning icon designed by Prosymbols; and steps icon designed by Freepik, all from Flaticon (www.flaticon.com). A.R. discloses support for the research of this work from the European Union – NextGenerationEU through the National Recovery and Resilience Plan (NRRP), Mission 4 Component 2 Investment 1.3—Call for tender No. 1561 of 11.10.2022 of Ministero dell'Universita' e della Ricerca (MUR). The project is identified by Project code PE0000021, Concession Decree No. 1561 of 11.10.2022 adopted by MUR, CUP—E13C22001890001, according to attachment E of Decree No. 1561/2022, and Project title "Network 4 Energy Sustainable Transition—NEST (Spoke 3)". Furthermore, K.V. discloses support for the research of this work from the European Union's Horizon 2020 research and innovation program under grant agreement N810755.

Author contributions

Conceptualization: A.R. and K.V.; Methodology: A.R., K.R., A.B. and K.V.; Formal analysis: A.R., G.M.M.P., A.B., L.G., M.C-B. and K.V.; Investigation: A.R., G.M.M.P., K.R., L.G., M.C-B. and K.V.; Software: A.R., G.M.M.P., A.B.; Resources: A.R. and K.V.; Writing—original draft: A.R. and K.V.; Writing—review and editing: A.R., K.R., A.B., L.G., M.C-B. and K.V.; Visualization: A.R and K.V.; Supervision: A.R., M.C-B. and K.V.; Project administration: A.R and K.V.; Funding acquisition: A.R and K.V.

Competing interests

The authors declare no competing interests.

Additional information

Supplementary information The online version contains supplementary material available at https://doi.org/10.1038/s41467-026-75309-w.

Correspondence and requests for materials should be addressed to Angela Re or Kaspar Valgepea.

Peer review information *Nature Communications* thanks the anonymous reviewers for their contribution to the peer review of this work. A peer review file is available.